

# The role pickup ions play in the termination shock

*Thesis submitted in partial fulfillment of the requirement for the degree of master of science  
in the Faculty of Natural Sciences*

Submitted by: **Daniel Ariad**

Advisor: **Prof. Michael Gedalin**

Department of Physics

Faculty of Natural Sciences

Ben-Gurion University of the Negev

July 17, 2012

# The role pickup ions play in the termination shock

*Thesis submitted in partial fulfillment of the requirement for the degree of master of science  
in the Faculty of Natural Sciences*

Submitted by: **Daniel Ariad**

Advisor: **Prof. Michael Gedalin**

Department of Physics

Faculty of Natural Sciences

Ben-Gurion University of the Negev

Signature of student:

Date:

Signature of supervisor:

Date:

Signature of chairperson of the committee for graduate studies:

Date:

July 17, 2012

# Abstract

The solar wind blows outward from the Sun and forms a bubble of solar material. The interaction of the solar wind with the local interstellar medium (ISM) results in a termination shock (TS). The TS marks the transition where the solar wind slows from supersonic to subsonic speed with respect to the surrounding ISM. The TS is a weak, quasi-perpendicular shock with broad regions on both sides that are populated by high energy ions and electrons. It seems that energetic particles play an important role in the formation of the TS structure, which distinguishes it from planetary bow shocks. The aim of this research is to consider the contribution of pickup ions to the energetic particles distribution at the TS. In this work a new method to calculate the particles velocity distribution at the downstream, assuming a known the upstream distribution, is introduced.

# Contents

<b>1</b>	<b>Introduction</b>	<b>5</b>
1.1	Scientific background . . . . .	5
1.2	Thesis Outline . . . . .	8
1.3	Fundamental concepts . . . . .	9
1.3.1	Magnetohydrodynamics, Discontinuity boundaries and Rankine-Hugoniot relations . .	9
1.3.2	Shock Waves . . . . .	14
1.3.3	The solar wind and the termination shock . . . . .	17
1.3.4	Interstellar pickup ions . . . . .	19
1.3.5	The shock dissipation mechanism . . . . .	23
1.3.6	Space observations and Voyager 2 spacecraft . . . . .	26
<b>2</b>	<b>The shock magnetic and electric fields</b>	<b>29</b>
<b>3</b>	<b>A numerical method to evaluate ions velocity distribution</b>	<b>36</b>
<b>4</b>	<b>The solar wind missing energy paradox</b>	<b>41</b>
<b>5</b>	<b>Examination of the pickup ions as a possible solution</b>	<b>49</b>
<b>6</b>	<b>An open question - the long tail observed by V2's LECP instrument</b>	<b>59</b>
<b>7</b>	<b>Conclusions</b>	<b>68</b>
<b>A</b>	<b>The equations of motion in the TS boundaries</b>	<b>71</b>
<b>B</b>	<b>Building a three dimensional grid</b>	<b>74</b>
<b>C</b>	<b>The roots of the equations of motions for a test particle in constant fields</b>	<b>76</b>

# Chapter 1

## Introduction

### 1.1 Scientific background

Recent observations of the termination shock [5, 51, 42, 8] have revealed that at this shock most of the energy of the incident ions is converted not into the downstream heated ion distribution but into high energy particles [33, 8], which are (presumably) pick-up ions accelerated at the shock itself [51, 13]. It seems that it is these particles, instead these of the SW, that ensure maintenance of the shock profile by making possible Rankine-Hugoniot relations. Respectively, the energetic particles are, at least partially, responsible for the shock structure.

Collisionless shocks, which are observed in the inner heliosphere, are not accompanied with energetic particles of such high energy density, as is observed at the termination shock. Yet, superthermal particles are quite common at interplanetary shocks [21, 45, 40, 38, 28, 27].

Measurements of the Termination Shock (TS) were made by Voyager 2 (V2) on 31 August 1 September 2007 at a distance of 83.7 au from the Sun. Data from the plasma and mag-

netic field instruments on V2 revealed that downstream the shock the heliosheath flow is not subsonic with respect to the thermal plasma. This indicated that non-thermal ion distributions probably have key roles in dynamical processes at the termination shock and in the heliosheath. [42]. That lead to a speculation that unobserved energetic particles with energies that fall in the instruments energy gap contain the missing energy.

Heliosheath energetic neutral atoms produced by charge exchange of suprathermal ions with interstellar neutral atoms were detected and mapped by STEREO A and B spacecraft from June to October 2007. Their energy spectra resemble those of solar wind pickup ions indicating that their parent ions are pickup ions energized by the termination shock. Their energy spectra entail that termination-shock-energized pickup ions contain the missing energy dissipated in the termination shock, and they dominate the pressure in the heliosheath. [51]

Using a test particle approach, it was shown that for a sufficiently strong cross-shock potential and sufficiently narrow shock ramp, shock drift acceleration mechanism can produce particles with enough energy to account for the "missing" energy of the downstream SW plasma at the termination shock. [7].

Recent observations of the structure of the termination shock [5] , plenty of interplanetary shocks [43, 44] , and of the suprathermal particles in the heliosphere [40, 28, 27] emphasized the necessity to comprehensively address the long-standing problem of the inter-relation of the shock structure and distribution of the accelerated particles [31, 53, 23] . Much effort has been invested so far into understanding of processes of pickup acceleration at quasi-perpendicular shocks [32, 55, 57, 35, 12, 14, 13] , yet the research so far lacks the necessary synthesis of theory and observations. The influence of the high-energy distributions on the shock structure has not been consistently studied yet. This issue became acute with the discovery of the first shock where these energetic particles provide the main part of the ion

pressure, and is extremely important for understanding of astrophysical shocks.

Finally, understanding the interaction of the heliospheric shocks with high-energy populations is extremely important for understanding the propagation of energetic particles in the heliosphere [9, 24, 10, 11] .

## 1.2 Thesis Outline

In chapter 2, we introduce the TS structure as observed by V2 and distill a magnetic and electric profiles. The electric profile is built upon the magnetic profile under ideal MHD assumption. In chapter 3, a numerical method to find the downstream velocity distribution based on the one at the upstream is derived. This is made by building a Liouville mapping between the shock two side is developed. Then in chapter 4, we determine the cross shock potential by applying the method to the SW and requiring that the downstream SW velocity, density and temperature will fit the observations. The downstream momentum transfer tensor is inferred from the evaluated distribution and the energy paradox, that motivates the study, is shown to hold also in the numerical calculation. In chapter 5, we check the possibility that PUI, which were not detected by V2, can solve the paradox by gaining the missing energy and satisfy the Rankine-Hugoniot relations. Observations of a high energy tail in the ions energy distribution are shown in chapter 6. This observation did not emerge in the numerically deduced distribution and possible directions for a modest correction are pointed out. Chapter 7 presents principle conclusions of the analysis and suggestions for future work on the subject.

## 1.3 Fundamental concepts

### 1.3.1 Magnetohydrodynamics, Discontinuity boundaries and Rankine-Hugoniot relations

The magnetohydrodynamic (MHD) theory is used to describe the behavior of a group of charged particles. A collection of charged particles can be treated as a conducting fluid, if the particle density is high and collisions occur frequently. Space plasmas are collisionless, which means that they are either so rarefied or hot that Coulomb collisions between the constituent particles happen so infrequently that they do not play an important role. Fortunately, the presence of a magnetic field replaces the role of collisions in "binding" the particles of the plasma together. To an extent in certain limits, collisionless dominated plasma system can be described by a MHD fluid theory.

Fluid dynamics deals with macroscopic phenomena where matter is treated generally as a continuum and deformable. MHD is a branch of continuum mechanics that deals with the motion of electrically conducting material in the presence of electromagnetic fields. Fluid dynamics treats a group of particles as an entity and assumes the particles are non-interacting. MHD also ignores the identity of individual particles and considers only the fluid elements. The motion of an ensemble of these particles constitutes a fluid motion.

The fundamental concept behind MHD is that magnetic fields can induce currents in a moving conductive fluid, which in turn creates forces on the fluid and also changes the magnetic field itself. MHD theory is designed to describe the physics of macroscopic phenomena. Hence, MHD theory has been used for explaining space structures that are much larger than the ion gyroradius and variations that occur with time scales much slower than the ion gyration period. The SW consists of collisionless plasma (plasma in which particles

interact through the mutually induced space-charge field, and collisions are assumed to be negligible) since its density is very low and, therefore, MHD theory only roughly describes it.

The foundations of the macroscopic equations are the moments of the Vlasov equation given by the following equation.

$$\frac{1}{2}m_s \int_{-\infty}^{+\infty} v^n \left( \frac{\partial f_s}{\partial t} + \mathbf{v} \cdot \nabla f_s + \mathbf{a} \nabla_v f_s - \frac{\delta f_s}{\delta t}_{\text{collision}} \right) dv^3 = 0 \quad (1.1)$$

where  $s$  index stands for the particle specie,  $n$  is the moment number and the expression in the bracket is the Vlasov equation. For clarity, in what follows we shall neglect the specie subscript.

The zeroth moment equation yields the continuity equation

$$\frac{\partial n}{\partial t} + \nabla(n\mathbf{V}) = 0 \quad (1.2)$$

where  $n$  is the particles density and  $\mathbf{V}$  is the flow velocity.

The continuity equation can be used to find the mass flux that crosses through a boundary. A boundary is an interface that separates the different regions of space. A large-scale plasma boundary can be defined through discontinuous macroscopic parameters such as density and temperature. However, plasmas are coupled to electric and magnetic fields and, therefore, the requirements must also include the behaviour of discontinuous electromagnetic fields. The complete set of discontinuous variables in collisionless plasma fluids includes the mass density, flow velocity, pressure tensor, current and electromagnetic fields. The Rankine Hugoniot Equations (RH) gives the jump condition between the two sides of the discontinuity for the quantities mentioned above.

In the case of no time dependence the equation reduces to  $\nabla(n\mathbf{V}) = 0$ . Integrating and

applying Gauss' theorem to conservation equation of mass flux over a volume which contain two regions separated by a boundary, yields the RH equation for mass flux conservation.

$$[G] \equiv [n m U \cdot \hat{\mathbf{n}}] = 0 \quad (1.3)$$

where the square brackets denote the difference between the values of total momentum flux in the two sides of the boundary.  $\rho$  is the mass density,  $n$  is the particles density and  $\hat{\mathbf{n}}$  is the shock normal. The integral states that the mass flux entering one side in the normal direction is equal the mass flux leaving the other side in the normal direction.

A simple classification scheme originally proposed by L.D. Landau and E.M. Lifshitz is given below.

$$\begin{aligned} \text{Tangential Discontinuity} & \quad G = 0 \quad B_n = 0 \\ \text{Contact Discontinuity} & \quad G = 0 \quad B_n \neq 0 \\ \text{Perpendicular Shock} & \quad G \neq 0 \quad B_n = 0 \\ \text{Parallel Shock} & \quad G \neq 0 \quad B_t = 0 \\ \text{Oblique Shock} & \quad G \neq 0 \quad B_n \neq 0 \\ \text{Rotational Discontinuity} & \quad G \neq 0 \quad B_n \neq 0 \end{aligned} \quad (1.4)$$

The MHD boundaries are organized according to whether a fluid crosses a boundary or not and whether a boundary supports a magnetic field normal to it. [39]

The the second Vlasov moment, known as conservation equation of momentum density, is

$$\frac{\partial}{\partial t} (\Pi_k + G_k) + \frac{\partial}{\partial x_i} (\Pi_{ik} + T_{ik}) = 0 \quad (1.5)$$

Where the momentum transfer tensor that is given by

$$\Pi_{ik} \equiv \int m v_i v_k f(\mathbf{r}, \mathbf{v}, t) d^3v \quad (1.6)$$

$T_{ik}$  is defined as the electromagnetic stress,

$$T_{ik} = \left( \frac{\epsilon_0 E^2}{2} + \frac{B^2}{2\mu_0} \right) \delta_{ik} - \left( \epsilon_0 E_i E_k + \frac{B_i B_k}{\mu_0} \right) = 0 \quad (1.7)$$

$G_k$  is the momentum density of the electromagnetic field (Poynting vector),

$$G_k = \epsilon_0 \mu_0 (\mathbf{E} \times \mathbf{H})_k = \frac{(\mathbf{E} \times \mathbf{H})_k}{c^2} \quad (1.8)$$

and  $\Pi_k$  is the average momentum vector,

$$\Pi_k \equiv \int m v_k f(\mathbf{r}, \mathbf{v}, t) d^3v \quad (1.9)$$

A full derivation of the equations above can be found at Parks 2003 [39].

In a stationary case, Integrating the conservation equation of momentum density over a volume  $V$ , bounded by surface  $S$ , that contains two regions separated by a boundary, yields the RH equation for momentum conservation across the boundary. The integral states that total momentum (mechanical plus electromagnetic) flux that flows out of the volume equals the total flux flowing in.

$$[\Pi_{ik} + T_{ik}] \cdot n_i = 0 \quad (1.10)$$

where the square brackets denote the difference between the values of total momentum flux in the two sides of the boundary. In a NIF with an electric field which is equal in both sides, a simplified vectorial form can be deduced

$$[\Pi_{1k} + \frac{B^2}{2\mu_0} \delta_{1k} - \frac{B_1 B_k}{\mu_0}] = 0 \quad (1.11)$$

We shall denote this vector as momentum transfer vector.

A further simplification can be made if:

1. The distribution function is gyrotropic,  $\langle v_i v_j \rangle = 0$  when  $i \neq j$ . In this case the ions gyration phases are random and hence uncorrelated.
2. The pressure tensor is isotropic, the tensor is diagonal and all components are equal.

3. The stress tensor is components are negligible relative to the corresponding components of the momentum transfer tensor.

In this case only the first component of the momentum transfer vector is non zero and the Rankine-Hugoniot relation for momentum conservation can be expressed in terms of thermal and kinetic energy.

In order to express the momentum conservation equation in that simplified form, one should notice that the momentum transfer tensor can be written in terms of the pressure tensor and kinetic energy density tensor as follows,

$$\Pi_{ij} = P_{ij} + mnU_iU_j \quad (1.12)$$

where the pressure tensor,  $P_{ij}$  is defined as

$$P_{ij} \equiv nm \langle w_i w_j \rangle = \sum \int m w_i w_j f d^3v \quad (1.13)$$

$\mathbf{w}$  is the thermal velocity,  $w \equiv \mathbf{v} - \mathbf{V}$  and  $\mathbf{V}$  is the stream velocity.

Using the relation above, neglecting the contribution of the stress tensor, the non-vanishing component of the momentum transfer vector can be written as

$$\left[ \frac{1}{3}nE_{th} + nE_k \right] = 0 \quad (1.14)$$

where we have used the fact that the pressure is isotropic to rewrite it in terms of thermal energy.

Since in collisionless plasma, the particle distribution function can take almost any form we express the thermal energy by taking the second velocity moment of the distribution function.

$$E_{th} \equiv \frac{1}{2}m \langle (\mathbf{V} - \langle \mathbf{V} \rangle)^2 \rangle = \int \frac{1}{2}m (\mathbf{V} - \langle \mathbf{V} \rangle)^2 \frac{f}{n} d^3v \quad (1.15)$$

where  $m$  is the proton mass,  $n$  is the proton density,  $f$  is the ion velocity distribution function,  $\mathbf{V}$  is the ion velocity and  $\langle \mathbf{V} \rangle$  is the downstream flow velocity. The kinetic temperature (or just temperature) of the plasma is defined in terms of the thermal energy as

$$\frac{1}{2}m \langle (\mathbf{V} - \langle \mathbf{V} \rangle)^2 \rangle = \frac{3}{2}kT \quad (1.16)$$

### 1.3.2 Shock Waves

Boundaries are formed when a flowing encounters an obstacle in its path. When the flow speed is supersonic shock waves or simply shocks are formed. A shock is an irreversible (entropy-increasing) wave that causes a transition from supersonic to subsonic flow as consequence of compressibility effects; that is, there is a velocity decrement and a density increment.

Space shocks are produced by collisionless plasmas and appear in two forms - steady-state shocks, for example bow shocks produced by the solar wind interacting with planets, and transient shocks, produced for example by solar flares and supernova explosions. They are classified by the angle  $\theta_{Bn}$  between the normal of the shock and the magnetic field. If angle is  $0^\circ$  or  $90^\circ$  the shock is considered parallel or perpendicular, respectively. Otherwise, the shock is considered oblique.

In the small-amplitude limit, the profile of a MHD wave does not change as it propagates, but even a small-amplitude wave will eventually distort due to wave steepening. The wave steepening happens when gradients of pressure, density, and temperature become so large that dissipative processes (e.g. viscosity, thermal conduction) are no longer negligible. In the steady state, a steady wave-shape - a shock wave - is formed in which the steepening effect of non-linear convective terms balance the broadening effects of dissipation. The shock waves

move at speeds larger than the ambient intrinsic speed. The dissipation inside the shock front leads to a gradual conversion of the energy being carried by the wave into heat. In plasma the situation is complicated by the fact that there can be several types of adiabatic waves or simply waves. [46]

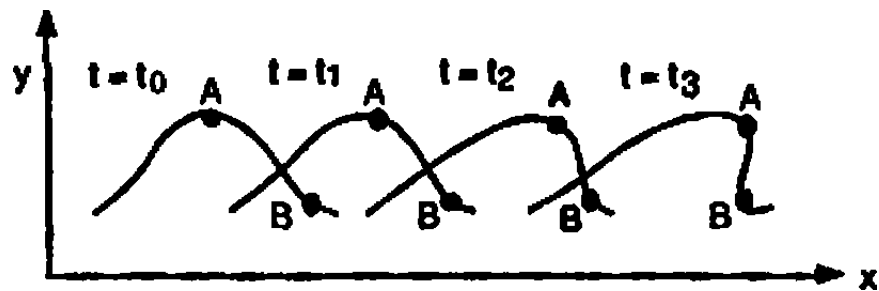


**Figure 1.1:** Illustration of how a compressional wave steepens to form a shock wave.

The best-known example wave steepening phenomenon is ocean waves that form breakers on the shore. In shallow water, the speed of surface waves is dependent on the depth of the water. An incoming ocean wave has a slightly higher wave speed near the crest of each wave than near the troughs between waves, because the wave height is not infinitesimal compared to the depth of the water. The crests overtake the troughs until the leading edge of the wave forms a vertical face and spills over to form a turbulent shock (a breaker) that dissipates the wave's energy as sound and heat.

When the plasma is perfectly conducting (infinite conductivity) the MHD equations that describe it are called Ideal MHD. The assumption of Ideal MHD fluid makes dissipative effects not possible, hence, it can only produce an infinitesimally thin shock. Shocks in this case have no structure. However, the formulation can describe steepening of the waves and the changes that occur in the fluid properties across the discontinuities.

In Ideal MHD there are three fundamental small-amplitude waves: the fast, intermedi-

ate, and slow modes. Because of the different characteristic speeds, there have dissimilar strengths. The strength of a shock is characterized by a Mach number, which is defined as the ratio between the shock velocity with respect to the flow and the wave speed ahead of the shock. If the shock moves much or slightly faster than the wave speed, it is called a strong or weak shock, respectively. MHD theory further delineates shocks as subcritical (supercritical) if their Mach number is smaller (bigger) than 2 to 3. Use is also made of the parameter  $\beta$  of plasma, which is defined as the ratio between the thermal and magnetic pressures ( $\beta = nk_bT/(B^2/2\mu_0)$ ).

The phase speed of the intermediate mode is given by

$$V_i^2 = V_A^2 \cos^2 \theta \quad (1.17)$$

where  $V_A = B/(\mu_0\rho)^{1/2}$  is the alfvén speed and  $\theta$  is the angle that the propagation vector  $\mathbf{k}$  makes with the magnetic field  $\mathbf{B}$ . The phase speed of the other two modes is given by

$$2V_{ph}^2 = (C_s^2 + V_A^2) \pm [(C_s^2 + V_A^2)^2 - 4C_s^2V_A^2 \cos^2 \theta]^{1/2} \quad (1.18)$$

Here  $C_s = (\gamma p/\rho)^{1/2}$  is the speed of sound ( $p, \rho$ , and  $\gamma$  are the pressure, mass density, and the ratio of specific heats, respectively). The phase speed of the fast ( $V_f$ ) and slow ( $V_s$ ) modes corresponds to the faster (+ sign) and slower (- sign) phase speeds given above.

After investigating many quasi-perpendicular shocks it was suggested that they all have a similar structure. As shown in the figure below, the field has a single sharp jump called ramp, but it is preceded by a gradual rise called the pedestal or foot. The thickness of the foot equals the distance to which protons are reflected by the shock before drifting through it. Also, the field right at and behind the ramp is higher than its eventual downstream value, and this is called the overshoot. Sometimes, the shock also consists a undershoot which follows the overshoot with a field that is that is lower than its eventual downstream value [26].

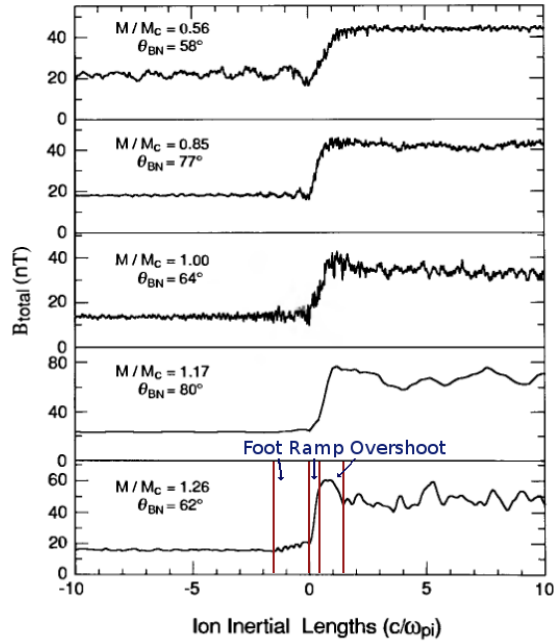


**Figure 1.2:** Observations of magnetic field magnitude for five quasi-perpendicular shocks ranging from subcritical to slightly supercritical. The measured temporal profile has been transformed to a distance scale using simultaneous measurements from a companion spacecraft that observed these shocks moments later.

The figure above shows example of several shocks ranging from subcritical to slightly supercritical. The top two subcritical shocks have simple ramps from upstream to down, with little or no foot or overshoot. However, both these shocks have standing precursor waves that are stationary in the shock frame. At shorter wavelengths, both shocks have small-amplitude propagating waves. The appearance of all these wave are controlled by the angle between the magnetic field and the shock normal. At higher Mach numbers, an overshoot and shock foot appear.

### 1.3.3 The solar wind and the termination shock

The solar wind (SW) is a stream of charged particles ejected outward from the upper atmosphere of the Sun. The SW is created mainly due to huge pressure difference between the hot plasma at the base of the corona and the interstellar medium (ISM). The pressure difference is due to the gravitational and thermal energies between the Sun's corona, extended outer layer, and the ISM. The very low pressure of the ISM acts as "vacuum cleaner", which "sucks out" the plasma from the solar corona, despite the restraining influence of the solar gravity. Thermal collisions in corona have significant role in shaping the velocity distribution which is described by a Maxwellian distribution.

Elementary fluid dynamics tells us that when one opens a gas reservoir filled with stationary gas to vacuum the gas outflow will be sonic at the surface of the reservoir and it accelerates outward - This outflow is driven by the large pressure gradient force. The addition of solar gravity introduces a retarding (backward) force reducing the outward expansion of the corona. This retarding force rapidly reduces with increasing distance from the Sun.

The effect of the retarding force is that the sonic point moves outward. The outflow starts subsonically and undergoes a sonic transition at a distance where the gravitational potential and kinetic energy of the random motion are equal. However, if there is a finite pressure in the surrounding ISM, the coronal expansion must eventually decelerate and stop where the SW pressure becomes equal to the interstellar pressure. The area in the heliosphere, the bubble blown into ISM, where the solar wind slows down to subsonic speed is called the termination shock (TS). [20, 39]

Similar shocks can be seen in terrestrial systems. A two-dimensional analogy may be seen by simply running a water tap into a sink creating a hydraulic jump. Upon hitting the floor of

the sink, the flowing water spreads out at a speed that is higher than the local wave speed, forming a disk of shallow, rapidly diverging flow (analogous to the tenuous, supersonic solar wind). Around the periphery of the disk, a shock front or wall of water forms in which the water depth suddenly increases. Outside the shock front, the water moves slower than the local wave speed (analogous to the subsonic interstellar medium) and the water depth varies slowly along the radial direction (analogous to the SW density increment, which is not possible in water due to its incompressible nature).

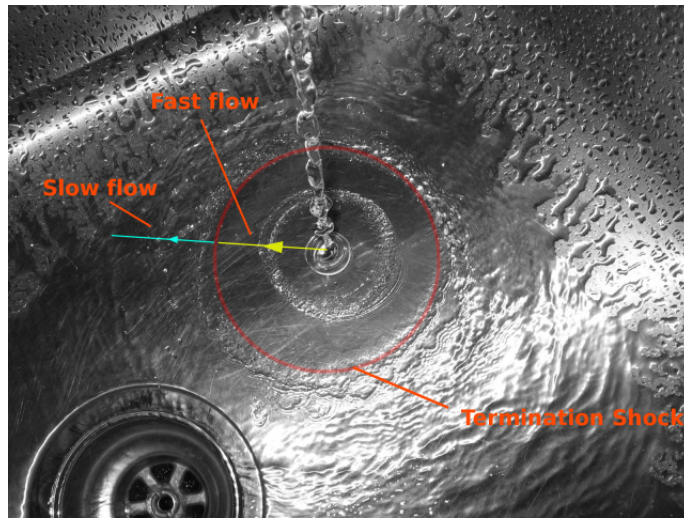


**Figure 1.3:** A termination shock in a sink basin.

It should be noted that the described hydrodynamic description above gives only a very simplified picture of the behaviour of the SW. The description above does not take into account electromagnetic effects. In addition, observations show the Sun is always dynamic and it may not be correct to assume the Sun's plasma is in thermal equilibrium. This has led to the consideration of kinetic SW models since hydrodynamic models are not capable of describing these dynamics phenomenons.

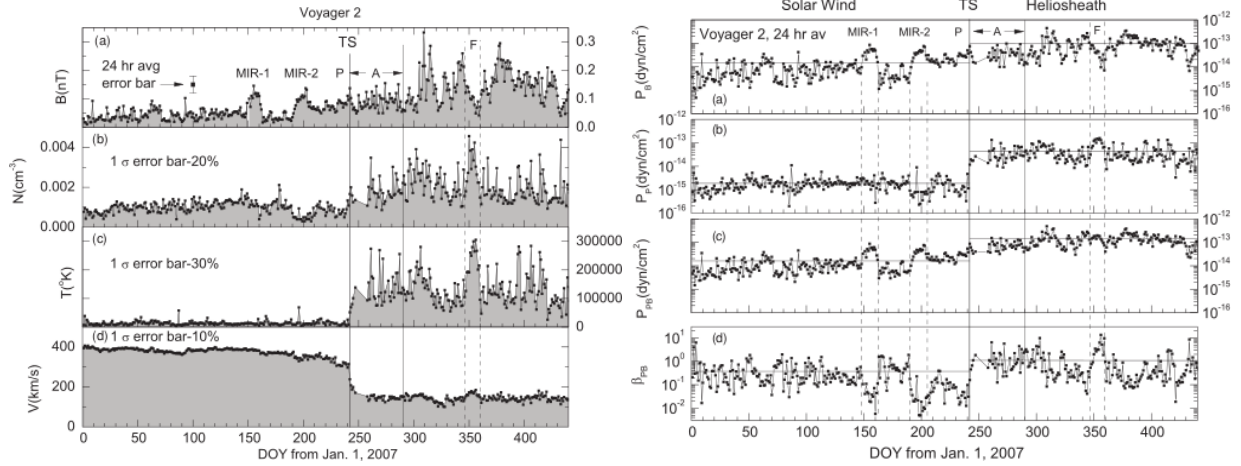


**Figure 1.4:** In the left side - Daily averages of magnetic field strength (a), plasma density (b), proton temperature (c), and bulk speed (d) measured by V2. In the right side - Daily averages of the magnetic pressure (a), the proton thermal pressure (b), the sum of the pressure and proton pressure (c), and the ratio of the proton pressure to the magnetic pressure (d) measured by V2.

[6]

### 1.3.4 Interstellar pickup ions

The heliosphere is moving with respect to the very local interstellar medium (VLISM) with relative velocity of about 26 km/s. Neutral atoms in the interstellar medium penetrate relatively freely into the heliosphere. Since the interstellar neutral gas is relatively cold ( $< 10^4 K$ ), both the thermal speed and the bulk speed of the interstellar neutral are negligible with respect to the SW speed. This means that the relative speed between the interstellar neutrals and the magnetized SW plasma is approximately the SW speed,  $u_{SW}$ .

Interstellar neutral particles can be ionized by photo-ionization, charge exchange with SW protons, or electron impact. All three ionization processes leaves the ions practically at rest with respect to the supersonic magnetized SW. These freshly born ions are picked up by the motional electric field of the SW flow. The initial ion trajectory is cycloidal, resulting from

superposition of gyration and drift. The velocity-space distribution at this early stage of the pickup ions (PUI) is a ring-beam distribution.

The ring-beam distribution of the new PUI represents an ion beam drifting through the SW plasma with velocity of  $v_{\parallel} = v_{SW} \sin \alpha$  toward the Sun along the direction of the magnetic field. All the ions in the beam are gyrating with a gyration speed of  $v_{\perp} = v_{SW} \cos \alpha$ , where  $\alpha$  is the angle between the SW velocity and the magnetic field vectors. This motion generates a broad spectrum of MHD turbulence which propagates, in a first approximation, with the SW flow velocity. The PUI interact with the self-generated MHD turbulence without significantly changing their energy. As a result of this process the pitch angle of the pickup ring particles become randomized in the SW frame. Their distribution becomes a pickup shell around the local SW flow velocity with a radius that equals the SW flow speed.

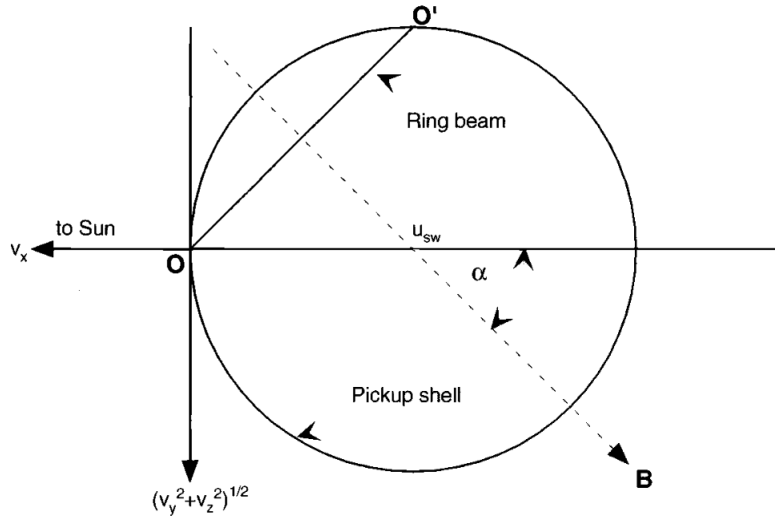


**Figure 1.5:** PUI phasespace distribution. The newly created ions are initially at rest, point O. It starts gyrating around the magnetic field, which is shown by the dashed line. The projection of the ring-beam is denoted by the OO' line.

The relatively rapid isotropization of the PUI on the pickup shell is followed by much slower processes changing the particle energy. The process is known as stochastic acceleration or second-order Fermi acceleration. The physical idea behind stochastic acceleration is quite simple. The heliosphere is filled with low-frequency MHD waves propagating along magnetic field lines. These noncompressive waves propagate near alfvén speed along the magnetic field line (sunward or antisunward). In the SW frame these waves have frequencies near the PUI gyration frequency and resonant wave-particle interaction occur. Since the MHD waves propagate in two opposite directions there are two scattered groups. The energy of each individual particle is conserved during the resonant interaction. However, in the SW frame the particle randomly gains or loses energy, depending on the directions of the particle and the MHD wave. This random energy diffusion process leads to stochastic acceleration (and deceleration) of the resonant particles. [37, 20]

Isotope	Density at TS ( $cm^{-3}$ )
$^1H$	$0.115 \pm 0.015$
$^4He$	$0.0153 \pm 0.002$
$^3He$	$(3.8 \pm 1.0) \times 10^{-6}$
$^{14}N$	$(8.0 \pm 1.3) \times 10^{-6}$
$^{16}O$	$(5.6 \pm 0.8) \times 10^{-5}$
$^{20}Ne$	$(9.2 \pm 2.0) \times 10^{-6}$

**Table 1.1:** Densities of atoms at the heliospheric TS ( 85 – 110 AU). The composition was observed by the Composition Spectrometer (SWICS) on both Ulysses and ACE. [19]

Vlasyliunas and Siscoe (1976) investigated the evolution of the PUI distribution in the absence of energy diffusion. Isenberg (1987) has since generalized this calculation by including energy diffusion [56, 22]. The PUI distribution function  $f(v, r)$  is a function of heliocentric

distance  $r$  which is measured in the observer frame, and particle speed  $v$  measured in the SW frame. In a steady, spherically symmetric expanding SW, an isotropic distribution of PUI evolves according to the following PUI transport equation -

$$\frac{\partial f}{\partial t} + u \frac{\partial f}{\partial r} - \frac{2uv}{r} \frac{\partial f}{\partial v} = \frac{1}{v^2} \frac{\partial}{\partial v} \left( v^2 D \frac{\partial f}{\partial v} \right) + \frac{n_H}{\tau_{ion}} \frac{\delta(v-u)}{4\pi v^2} \quad (1.19)$$

where  $u$  is the SW speed,  $n_H = n_H^\infty \exp(-\lambda\theta/r \sin\theta)$  is the density of interstellar neutral hydrogen that penetrates the SW, and  $\tau_{ion} = \tau_{ion}^0 r^2/r_0^2$  is the ionization frequency of interstellar neutral hydrogen largely due to charge exchange with SW protons and due solar ultraviolet radiation.  $\theta$  stands for the polar angle measured from the solar rotation axis and  $\lambda$  is a characteristic distance. It has been assumed that the isotropization of the initial ring-beam distribution is immediate so that the source term may be approximated as an isotropic shell moving at the solar wind speed. The equation is solved easily using the method of characteristics in the limit that  $D = 0$ . In this case, the steady-state solution is given by

$$f(r, v) = \frac{3}{8\pi} \frac{n_H(r_1)}{\tau_{ion}^0 u^2} \frac{r_0^2}{r} \left( \frac{u}{v} \right)^{3/2} H(u-v) \quad (1.20)$$

where  $r_1 = (r^2 v^3 / U^3)^{1/2}$ . For simple cold distribution it reduces to

$$f(r, v) = \frac{3}{8\pi} \frac{n_H^\infty}{\tau_{ion}^0 u^2} \frac{r_0^2}{r} \left( \frac{u}{v} \right)^{3/2} \exp\left(-\frac{\lambda}{r} \frac{\theta}{\sin(\theta)} \left( \frac{u}{v} \right)^{3/2}\right) \quad (1.21)$$

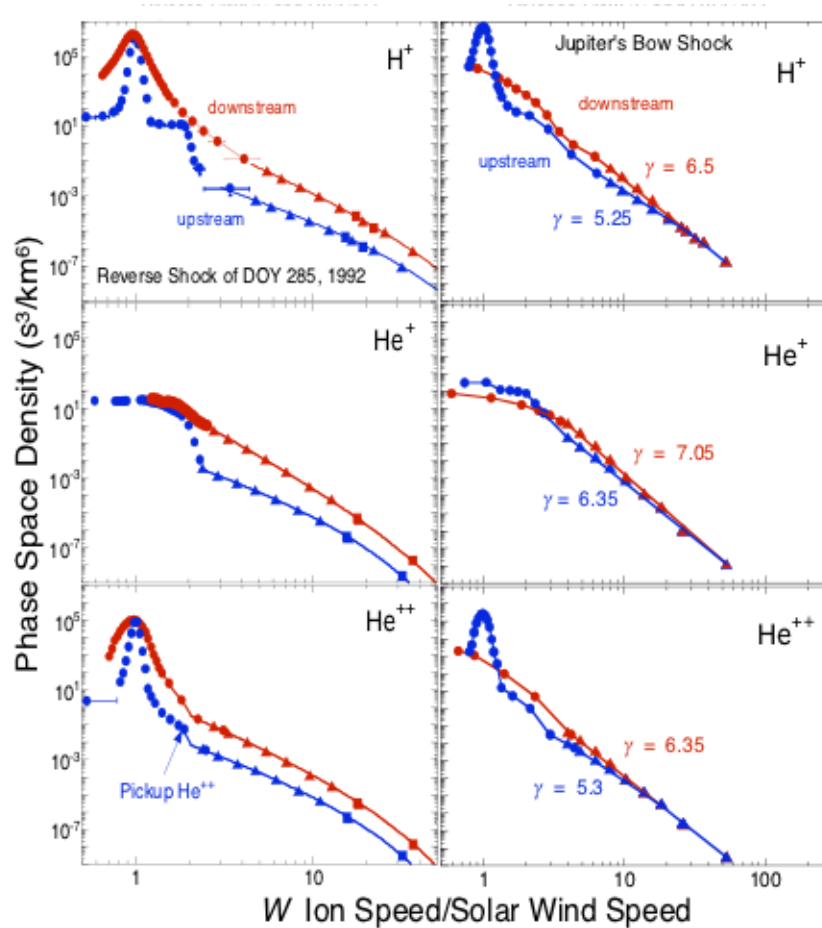


**Figure 1.6:** The tail portions of the  $He^+$  and  $He^{++}$  spectra derived from the HISCALE ion data could be separately determined because there was sufficient overlap between the SWICS and HISCALE data. On the left panel - the reverse shock of day 285, 1992. On the right panel - the Jovian bow shock of day 33, 1992 [18]

### 1.3.5 The shock dissipation mechanism

In shock there is irreversible dissipation, which can be described as transformation of flow kinetic energy into random thermal energy of the ions. In an ordinary fluid, the dissipation is provided by viscosity due to collisions between the molecules. The collisions redistribute the energy among all the particles, so that they all have the same temperature, irrespective

of their type. In collisionless plasma there must be other heating mechanisms, since the scale lengths of collisionless shocks are less than the mean free path between collisions [25].

The shock dissipation mechanism in collisionless shocks, which we consider, is based on particle dynamics at fixed macroscopic average fields. The disturbance by the microscopic fields, waves in the fields, is assumed to be neglectable in the dissipation time scale. However, it is the waves and turbulence that make the whole process irreversible and entropy increment.

In the absence of collisions, the electrons and ions in the plasma, which have very different characteristics, may not be heated by the same process. Observations show that the ions are heated much more than electrons at supercritical shocks [47]. The electrons contribution to the shock dissipation process is modest compared to that of protons.

Since ions mass is larger in three orders of magnitude than the electrons mass, ions have larger gyroradius and penetrate deeper into the shock deeper than electrons. Their different turning points create charge separation resulting an electric field, pointing upstream perpendicular to the shock surface. The field accelerates electrons through the shock and decelerates ions. The resulting potential created is called cross-shock potential. [30].

If the total energy of the ion exceeds the potential drop it penetrates the shock, otherwise it is reflected. Reflected ions gyrate about the upstream magnetic field with large gyroradius and surf in the direction of the motional electric field gaining energy from it. The ions may have multiple encounters with the shock until, finally, convected downstream. Another option for gaining energy is that an ion penetrate the shock but gyrate back upstream. Since the magnetic field downstream is larger than upstream, the ion gyroradius downstream is smaller than upstream. Hence, the work done, by the electric field perpendicular to the shock normal, on the ion in the upstream is larger than in the downstream region. This ion

will have an average advance in motional electric field direction. These two mechanisms are referred as Shock Drift Acceleration or Multiply Reflected Ions. [1, 55, 57]

We can describe the shock dissipation mechanism by a series composed by various combinations of three fundamental step [17]:

1. The ion transport thorough the shock from upstream to downstream.
2. The ion gyrates in downstream and transits through the shock in reverse direction into upstream.
3. The ion is specularly reflected off the shock in upstream, due to insufficient kinetic energy.

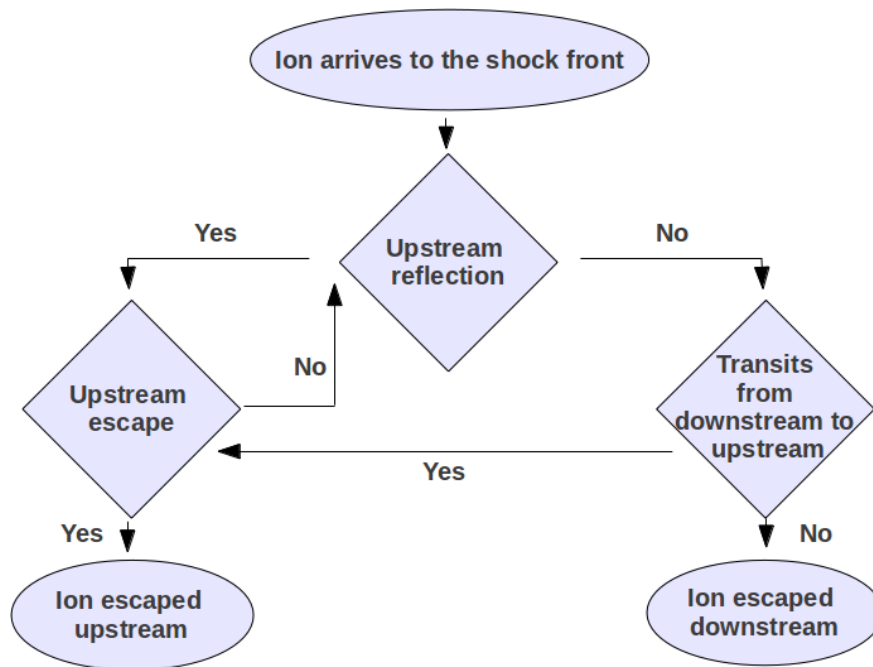


**Figure 1.7:** Flowchart of the dissipation mechanism.

The ions that encounter the shock are multiply reflected by the shock in a manner that results a deceleration in the average flow velocity and an increment in the flow temperature.

It is suggested that the SDA constitutes the main dissipation mechanism for collisionless shocks.

### **1.3.6 Space observations and Voyager 2 spacecraft**

Space observations are unique in that the smallest plasma scale (the Debye length) is usually larger than the spacecraft. This means that point measurements are possible because, in general, our measurement devices do not affect the plasma. This enable us to measure how the plasma changes as it passes through the shock and study the collisionless dissipation mechanisms in action.

Usually, the satellite has a very low speed relative to the sun. The shock also moves back and forth oftenly due to slight changes in the SW or LISM speed and density. The observations consist of time series for the different quantities, and if the speed of the shock relative to the satellite is constant, then the profiles we observe in time will be the same as the shock's profile in space.

The Voyager 2 (V2) spacecraft is a space probe launched by NASA on August 20, 1977 to study the outer Solar System and eventually interstellar space. On August 30, 2007, V2 passed the termination shock into the heliosheath at a distance of about 83.6 AU. Due to the variations of the solar wind dynamic pressure or waves on the shock front, the termination shock moved back and forth, and V2 crossed the TS multiple times and gathered a large amount of data about it.

Three scientific instruments that their data was used to study the proton distribution functions and the magnetic fields in TS are mentioned below.

1. Plasma Spectrometer (PLS) - The instrument consists of two Farady cup plasma de-

tectors: one pointed along and one at right angles to the Earth-spacecraft line. The Earth-pointing detector uses a geometrical arrangement that consists three Faraday cups, each of which views a different direction in velocity space. With this detector, values of plasma parameters (velocity, density, and pressure) can be obtained. The energy range for protons and for electrons is from 10 to 5950 eV. Two sequential energy per charge scans are employed with nominal values  $\Delta E/E$  equal to 29%, and 3.6%. The two scans allow the instrument to cover a broad range between subsonic ( $M < 1$ ) and highly supersonic ( $M \simeq 100$ ) flows; thus, significant measurements can be made in a hot planetary magnetosheath as well as in a cold SW. In addition, the use of two energy resolutions during the cruise phase of the mission allows simultaneously the measurement of solar wind properties and a search for interstellar ions.

The Earth-pointing detector cluster has an approximately conical field of view with a half angle  $90^\circ$ . The exceptionally large field of view makes this detector especially suited for use on a three-axis stabilized spacecraft. No mechanical or electric scanning is used. An additional sensor with a field of view perpendicular to that of the main cluster, is included to improve the spatial coverage for the drifting or corotating positive ions. This detector is also used to make measurements of electrons in the range 10 to 5950 eV. [4]

2. Triaxial Fluxgate Magnetometer (MAG) - The magnetic field experiment carried out on the V2 mission consists of dual low field (LFM) and high field magnetometer (HFM) systems. The dual systems provide greater reliability and, in the case of the LFM's, permit the separation of the spacecraft magnetic fields from the ambient fields. Additional reliability is achieved through electronics redundancy. In general, each component of the IMF hourly average has an uncertainty of up to (+/- 0.05 nT) in the region beyond 10 AU. [3]

3. Low Energy Charged Particle (LECP) - The low energy charged particle experiment employs a set of many solid state detectors arranged to characterize, with various levels of energy, directional, and compositional discriminations, the in-situ charged particle environment of the spacecraft. It can count the number of ions striking a particle detector per specified accumulation interval. The counted ions may be discriminated as to their energies and as to their ion composition. The instrument has an energy range of 0.028-3.5 MeV for protons divided to eight channels. [29]

In order to analyze the LECP observations, one must understand the relation between the V2 LECP equipment measurements (Counts) and the protons density per velocity. The relation is described below -

$$Counts = \sum_i \frac{n_i}{\Delta v_i} v_i \Delta v_i \Delta S \Delta t \xrightarrow{\text{Continuity Limit}} \Delta S \Delta t \int_{\Delta v} v f(v) dv \quad (1.22)$$

where  $f(v)$  is the density per velocity function,  $\Delta S$  is detector surface area and  $\Delta t$  is accumulation time.

We continue by Using the Jacobian transformation:

$$E = \frac{1}{2} m_p v^2 \Rightarrow v = \sqrt{\frac{2E}{m_p}} \Rightarrow dv = \frac{dE}{\sqrt{2m_p E}} \quad (1.23)$$

$$Counts = \Delta S \Delta t \int_{\Delta v} v f(v) dv = \Delta S \Delta t \frac{1}{m} \int_{\Delta E} f(E) dE \quad (1.24)$$

For sufficiently narrow energy passbands:

$$Particle \ density \ per \ velocity \ \approx \ m_p \frac{Counts}{\Delta E \Delta S \Delta t} \quad (1.25)$$

The parameters of V2 LECP's eight ion channels which need to substitute in the formula derived below are:

Effective Field of View (degrees): 45

Product of channel efficiency and geometric factor,  $\Delta S$  ( $cm^2 - ster$ ): 0.113

Total Accumulation Interval,  $\Delta t$  (sec): 192 (187.2 active time).

The energy passbands,  $\Delta E$  (MeV): 0.028–0.043, 0.043–0.080, 0.080–0.137, 0.137–0.215, 0.215 – 0.540, 0.540 – 0.990, 0.990 – 2.140, 2.140 – 3.500 .

# Chapter 2

## The shock magnetic and electric fields

During the days 242-244 of year 2007 V2 crossed the TS at heliographic inertial (HGI) coordinates<sup>1</sup> (83.66 AU,  $-27.5^\circ$ ,  $216.3^\circ$ ) at least five times (only during three of them telemetry was all right). Due to the variations of the solar wind dynamics pressure or waves on the shock front, the termination shock moved back and forth [5, 42]. We pick up the third telemetred shock crossing between 23:30 August 31 - 00:40 September 1, 2007 which have the best data coverage to fit a magnetic field profile.

Using the shock normal (0.986,0.165,0.032) and upstream SW velocity (321.01,11.26,1.07) m/s founded by Li. et al (2008), that used velocity-magnetic field coplanarity method suggested by Abraham-Shrauner (1972) with a Monte-Cralo method, we found that the SW flow projection along the shock normal is 99.1% of its magnitude. That means that we are almost in a normal incidence frame (NIF), so the shock normal and most of the upstream and downstream magnetic field components lie on the same plane. Another implication is that most of the change in the magnetic field is in the components perpendicular to the

---

<sup>1</sup>The HGI coordinates are Sun-centered and inertially fixed with respect to an X-axis directed along the intersection line of the ecliptic and solar equatorial planes. The Z-axis is directed perpendicular to and northward of the solar equator, and the Y-axis completes the right-handed set.

shock normal.

All the spacecraft magnetic field measurements are in Radial Tangential Normal coordinate system (RTN). RTN refer to a spacecraft centered coordinate system. where, R axis is along Sun to Spacecraft, T is along the vector product of Sun's spin axis and the radial axis and N completes the right-handed triad. The RTN does not vary in time significantly during the transition of the shock. The maximum variation angle of the R axis during days 201 to 247 relative to midnight of day 243 in year 2007 is less than 0.0013 rad so we can regard the axes directions as stationary during that time. The former result was found by comparing V2 hourly velocities during this period. The data was obtained from the JPL HORIZONS system and was evaluated by the Voyager Navigation Team in Feb 23, 1993, based on actual tracking data from 1990-Jan-23 to 1992-Oct-30.

In what follows we use the shock coordinate system (SCS) such that  $x$  axis is along the shock normal and  $y$  axis has a zero mean magnetic component in the shock. This is achieved by ordered rotations of 0.165, 0.031 and 1.798 rad around the  $z$ ,  $y$  and  $x$  axes, respectively.

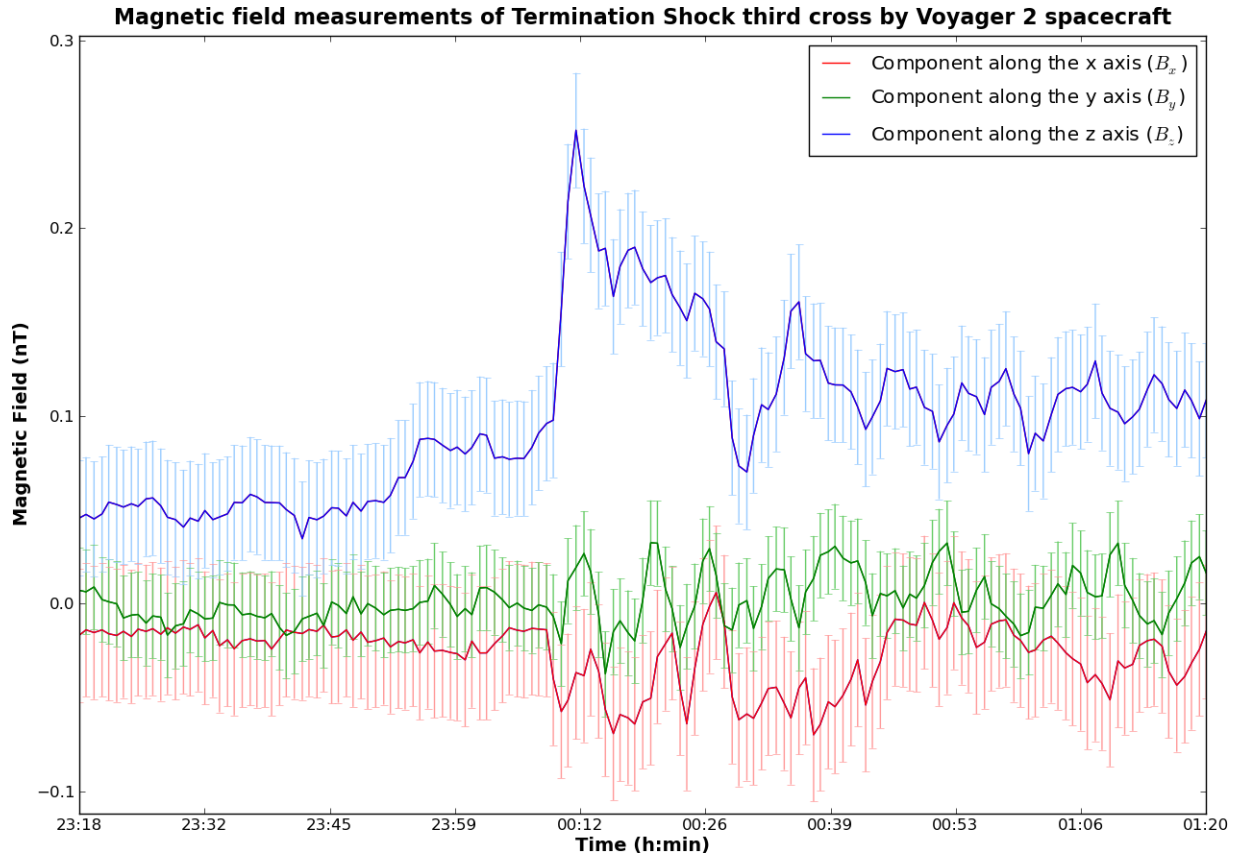


**Figure 2.1:** Magnetic field measured by Voyager 2 Triaxial Fluxgate Magnetometer (MAG) in CCS at 48 sec average.

As can be seen in figure 1, the shock is a quasi-perpendicular supercritical shock of a moderate strength with a "classical" structure consisting of a foot, ramp and overshoot. The shock structure observed by Voyager 2 is very complex due to large fluctuations as shown in the figure below, magnetic field magnitude detailed plot of 0.48 sec intervals [5].

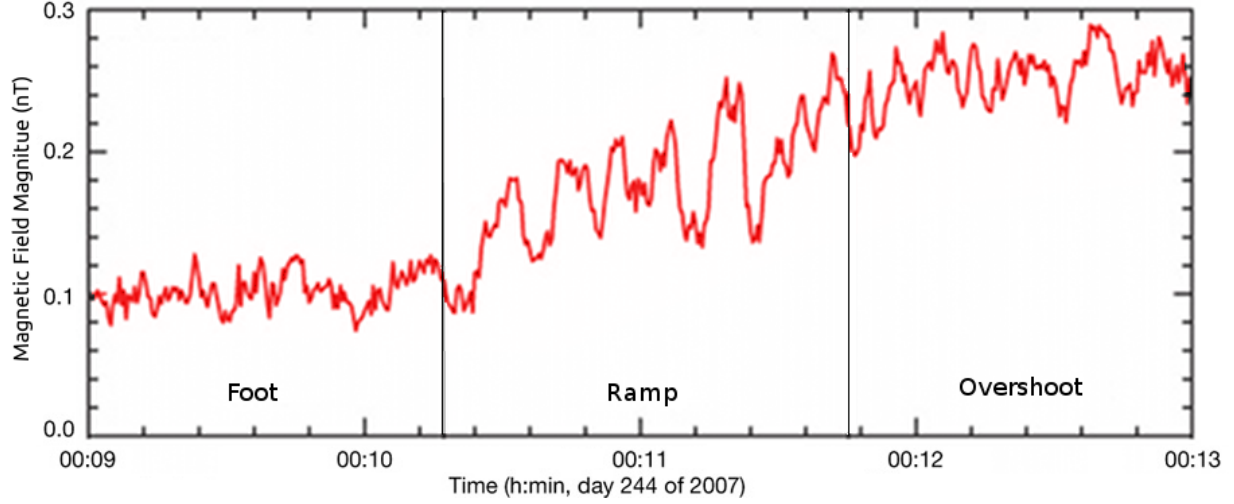


**Figure 2.2:** Magnetic field magnitude measured by Voyager 2 Triaxial Fluxgate Magnetometer (MAG) at 0.48 sec intervals. The MAG the vector magnetic field at rate of  $2.08 \text{ samples sec}^{-1}$

We fitted to the vector magnetic field measured by Voyager 2 magnetometer in SCS the following shock profile equation, following the principles of Gedalin [16]:

$$B_z(t) = B_u \sin \theta \left[ 1 + \left( \frac{R_f - 1}{2} \right) \left( 1 + \tanh 3 \frac{(t + t_0) + D_f - 3D_r}{D_f} \right) + \frac{R_r - R_f}{2} \left( 1 + \tanh \frac{3(t + t_0)}{D_r} \right) + (R_o - R_r) \exp \left( -2 \frac{((t + t_0) - D_o)^2}{D_o^2} \right) + \frac{R_d - R_r}{2} \left( 1 + \tanh 3 \frac{(t + t_0) - D_o - D_d}{D_d} \right) \right] \quad (2.1)$$

$$B_y(t) = 0 \quad (2.2)$$

$$B_x(t) = B_u \cos \theta \quad (2.3)$$

the parameters of the model fit:

$$B_u = 0.05 \times 10^{-9} \text{ T}, \theta = 70^\circ, D_d = 9.1 \times 10^{-3} \text{ days}, D_f = 1.2 \times 10^{-2} \text{ days}, D_o = 1.2 \times 10^{-3} \text{ days},$$

$$D_r = 1.5 \times 10^{-3} \text{ days}, R_d = 2.3 \text{ T}, R_f = 1.8 \text{ T}, R_o = 5.4 \text{ T}, R_r = 3.8 \text{ T}, l = 244 \text{ days}$$

Since  $\nabla \cdot \vec{B} = 0$ , the shock normal magnetic field component,  $B_x$ , is constant across a one-dimensional shock. Variations of  $B_x$  may indicate that the shock structure is not exactly one-dimensional and/or there are waves superimposed on the stationary profile. One has also to take into account that typically there are substantial errors in the determination of the shock normal direction. With only single spacecraft measurements it is difficult to estimate to what extent the shock is not one-dimensional and/or stationary. We shall stick to the above model approximation, shown in figure 3, which is based on the widely accepted description of the supercritical shock [48].

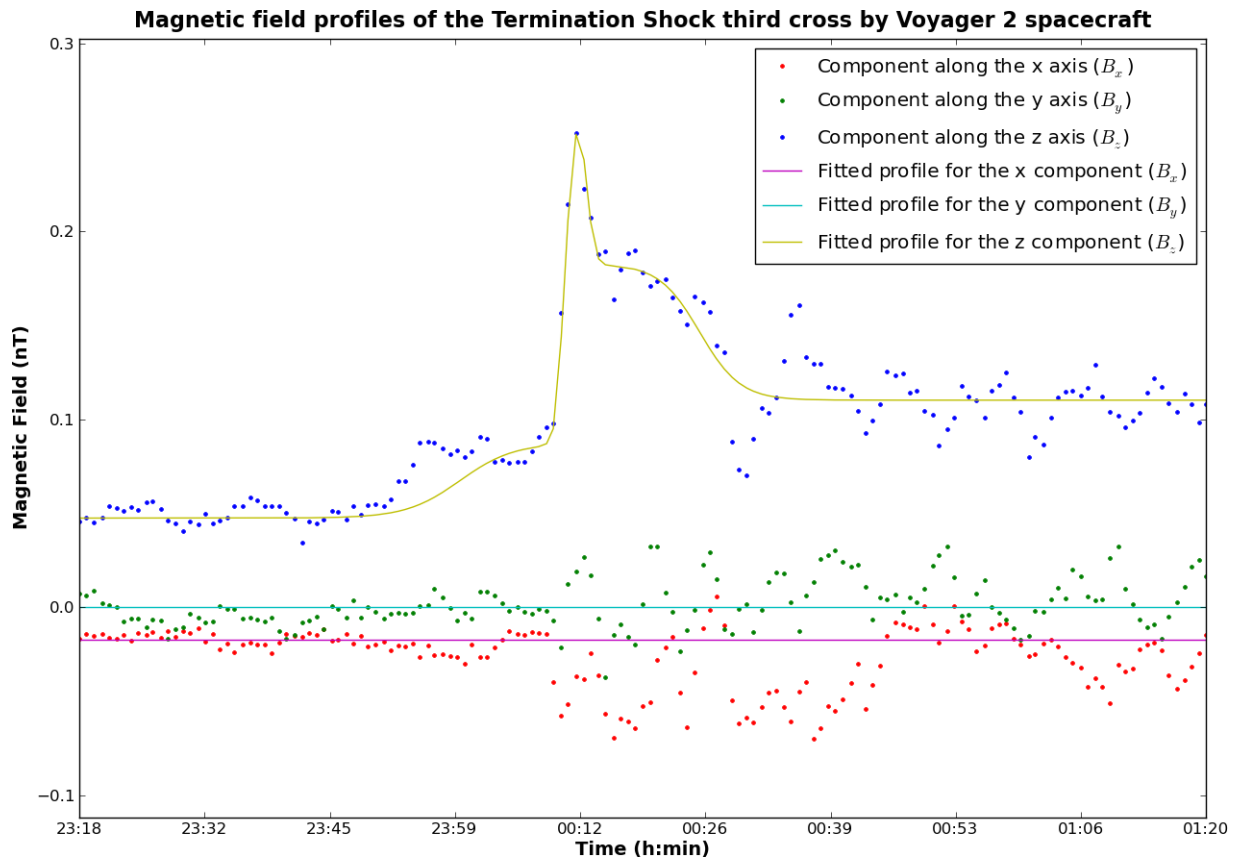


**Figure 2.3:** The fitted magnetic field profile to Voyager 2 MAG 48 sec averaged measurements.

Since we have the magnetic field vector as function of time, in order to transform it to a func-

tion of SCS we need to know the spacecraft and shock velocities. Although the first is 15.558 km/s in the radial direction, the last is unknown and therefore an approximate is needed. Richardson et al. estimated the shock speed relative to the spacecraft as  $54.4 \pm 17.3$  km/s ( $v = 4.7 \times 10^9$  m/day) forward to the sun using a method developed by Adolfo and Scudder (1986) [42]. For this shock velocity the overall shock width is 150,000 km which is about 3 times the ion upstream convective gyroradius, while the foot length approximately equals the convective gyroradius. For other planetary shocks the foot length does not exceed 0.7 ion convective gyroradius [36, 47]. Actually, one of the widely used methods to determine the terrestrial bow shock speed is to measure the time needed to cross the foot. Adopting the same approach we introduce the correction factor of 0.5 to the velocity estimation above,  $v$ . To get the fitted function depend on the displacement instead of time, we substitute  $t = x/v$  in the magnetic field equations.

The next part is to approximate the electric field. We assume for an estimate quasineutrality, electron current dominance. Our starting point is the ideal MHD fluid generalized Ohm's law with pressure tensor divergence that provides stationary fields and current as follows

$$\vec{E} = -\mathbf{U}_e \times \mathbf{B} + \frac{1}{n_e e} \mathbf{J} \times \mathbf{B} - \frac{1}{n_e e} \nabla \cdot \mathbf{P} \quad (2.4)$$

with maxwell equation,

$$\mathbf{J} = \frac{1}{\mu_0} \nabla \times \mathbf{B} \quad (2.5)$$

where  $\mathbf{U}_e$  is the electron flow velocity and  $\mathbf{P}$  is the electron pressure. since  $\nabla \times \mathbf{E} = 0$  for stationary fields then we must have  $-\frac{1}{n_e e} \nabla \cdot \mathbf{P} = (\mathbf{B} \cdot \nabla) \vec{B}$ .

we take the electric field model profile to be:

$$E_x = -\alpha \frac{B_u \sin \theta}{\mu_0 n_e e} \frac{\partial B_z}{\partial x} \quad (2.6)$$

or in terms of potential, which is merely the magnetic field shifted and rescaled.

$$\Phi = \alpha \frac{1}{\mu_0 n_e e} (B_z - B_u \sin \theta), \quad E_x = -\frac{\partial \Phi}{\partial x} \quad (2.7)$$

The two other components of the electric field stay constant along the shock.

$$E_y = U_x B_z \quad (2.8)$$

$$E_z = 0 \quad (2.9)$$

The parameter  $\alpha$  is a correction factor that was added since, even under the rough approximation of ideal MHD, not all the involved quantities were known. The electrons pressure is unknown and was excluded from the calculation. The factor is calibrated by the requirement that the downstream distribution moments (flow speed, temperature and density), calculated numerically by a method based on Liouville mapping and which is described in the next chapter, will fit the V2 observations. This approximation is widely used [54, 34].

We calibrate  $\alpha$  so the shock cross potential would be 93 eV which is %17 of the upstream flow kinetic energy, 538.558 eV. However, it is potential difference at the ramp that takes a major role in deflecting the ions. The reason lies in the fact that the ramp is narrow enough to make the ions gyration due to the magnetic field neglectable while the electric force is significant large. The ramp cross potential is 245 eV which is %45 of the upstream flow kinetic energy.

In what follows we adopt a normalization convention -  $\mathbf{u} \equiv \frac{\mathbf{v}}{U_u}$ ,  $\mathbf{b} \equiv \frac{\mathbf{B}}{B_u}$ ,  $\tau \equiv \Omega_u t$ ,  $\Omega_u = \frac{eB_u}{m_i}$ ,  $e_y = \frac{E_y}{U_u B_u} = \sin \theta$ . where  $U_u$ ,  $B_u$ ,  $E_u$ ,  $m_i$ ,  $e$ ,  $\Omega_u$  and  $\theta$  denotes the upstream values of SW flow speed, magnetic field, electric field, proton mass, electron charge, gyration frequency and the angle between the shock normal and the magnetic field, respectively.

To normalize the magnetic and electric field fitted functions we need to divide them with  $B_u$  and  $U_u B_u$ , respectively. In order that the functions will depend on a normalized argument we multiply it with  $V_u/\Omega_u$ . It is then instructive to look on the normalized z component of the

magnetic field with the  $x$  normalization factor concealed in four of the shock parameters and the upstream magnetic field hidden in the other four. Under this form the shock parameters have normalized units of magnetic field and length.

$$B_z(x) = \left[ 1 + \left( \frac{R_f - 1}{2} \right) \left( 1 + \tanh 3 \frac{x + D_f - 3D_r}{D_f} \right) + \right. \quad (2.10)$$

$$\left. \frac{R_o - R_f}{2} \left( 1 + \tanh \frac{3x}{D_r} \right) + (R_r - R_o) \exp \left( -2 \frac{(x - D_o)^2}{D_o^2} \right) + \frac{R_d - R_o}{2} \left( 1 + \tanh 3 \frac{x - D_o - D_d}{D_d} \right) \right] \quad (2.11)$$

The first group consists of  $R_f, R_r, R_o$  and  $R_d$  which are the foot, ramp, overshoot and undershoot heights, respectively. The second group consists of  $D_f, D_r, D_o$  and  $D_d$  which are related to the foot, ramp, overshoot and undershoot widths, respectively. The foot lies in  $-D_f < x < -D_r/2$ , ramp  $-D_r/2 < x < D_r/2$ , overshoot  $D_r/2 < x < (D_o + D_d)$  and undershoot  $(D_o + D_d) < x$ . It should be noted that here for convenience  $x = 0$  corresponds to middle of the ramp. There shock parameter values are  $D_f = 0.4, R_f = 1.7, D_r = 0.05, R_r = 5.1, D_o = 0.04, R_o = 3.6, D_d = 0.3, R_d = 2.2$ .

# Chapter 3

## A numerical method to evaluate ions velocity distribution

In this section we introduce a new method that evaluates numerically the downstream ions velocity distribution of the TS given that the distribution function is known upstream. This method will be verified by comparing the computation results with the V2 measurements.

In what follows we assume that the shock can be considered as one-dimensional and stationary, that is, the electric and magnetic fields depend only on the coordinate along the shock normal and do not depend on time. These approximations are justified by the observations that the typical time scale of the shock reformation is much larger than the proton gyration period while the shock curvature radius is much larger than the gyroradii of the energetic ions. Thus, we may treat the distributions as formed locally and instantaneously.

Let  $x$  be the coordinate along the shock normal. The collisionless Vlasov equation implies  $f(t, \mathbf{r}, \mathbf{v}) = \text{const}$  along the particle trajectory  $\dot{\mathbf{r}} = \mathbf{v}$ ,  $\dot{\mathbf{v}} = (e/m)(\mathbf{E} + \mathbf{v} \times \mathbf{B})$ . In the one-dimensional stationary case one has, respectively,  $f(x, \mathbf{v}) = f_0(x_0, \mathbf{v}_0)$ , where it is implied

that  $x_0, \mathbf{v}_0$  and  $x, \mathbf{v}$  belong to the same trajectory. Thus, one can build the ion distribution at the shock cross-section at  $x$  by tracing all possible trajectories back to the initial point  $x_0$  where the distribution is known. It is worth noting that the mapping is not one to one since an ion can cross the same cross-section more than once (this is what actually happens since ions gyrate in the magnetic field) and the coordinates  $y$  and  $z$  along the shock front are ignored. This does not pose any problem since all these crossings correspond to the same value of the distribution function.

The equations of motion of particles in average fields are time-reversible (if we replace  $t$  by  $-t$ , they will have the same form). For dissipation at a shock, we must have an irreversible process since entropy must increase. There is an additional process of scattering that ensures the irreversibility, which is caused by waves and turbulence. However, the effect of ion instabilities is neglectable in the considered time scale.

In view of all above, the proposed mode of operation is as follows. The phase space at some  $x$  downstream is divided by a three dimensional grid into sufficiently small cells. The velocity in the center of each cell,  $\mathbf{v}$ , is assigned to an ion, which is further traces backward to time until the trajectory reaches the place upstream,  $x_0$ , where the distribution is known. Then the cell is assigned the value of the distribution function corresponding to the velocity  $\mathbf{v}_0$  which the ion has in the point  $x_0$ . If the ion trajectory does not reach upstream this cell is considered empty.

We use a numerical approach as described below. First, we determine the downstream spectrum in interest. A good start can be the relevant spectrum range of the initial distribution. In case that measurements of average flow velocity and temperature downstream exist, the relevant area can be inferred. After defining the area in concern, we divide it into spherical volume elements. Bearing in mind that we are ultimately interested in the distribution  $F(v)$ ,

where  $v = |\mathbf{v}|$ , here we use the three dimensional grid in spherical coordinates in the velocity phase space,

$$v_x = v \sin \theta \cos \phi, \quad v_y = v \sin \theta \sin \phi, \quad v_z = v \cos \theta$$

The volume of the cell  $(\Delta v, \Delta \theta, \Delta \phi)$  is

$$\begin{aligned} \Delta V &= \int_{v-\frac{\Delta v}{2}}^{v+\frac{\Delta v}{2}} \int_{\theta-\frac{\Delta \theta}{2}}^{\theta+\frac{\Delta \theta}{2}} \int_{\phi-\frac{\Delta \phi}{2}}^{\phi+\frac{\Delta \phi}{2}} v'^2 dv' \sin \theta' d\theta' d\phi' = \\ &= \frac{\Delta \phi}{3} \left( \left( v + \frac{\Delta v}{2} \right)^3 - \left( v - \frac{\Delta v}{2} \right)^3 \right) \left( \cos \left( \theta - \frac{\Delta \theta}{2} \right) - \cos \left( \theta + \frac{\Delta \theta}{2} \right) \right) = \\ &= \frac{\Delta \phi}{3} \left( 2 \sin \theta \sin \frac{\Delta \theta}{2} \right) \left( 6 v^2 \left( \frac{\Delta v}{2} \right) + 2 \left( \frac{\Delta v}{2} \right)^3 \right) = \\ &= \Delta \phi \sin \theta \sin \frac{\Delta \theta}{2} \left( 2v^2 \Delta v + \frac{\Delta v^3}{6} \right) \end{aligned} \tag{3.1}$$

Respectively, this  $\Delta V$  should be used as a weighting factor when numerically determine values requiring summation or averaging. In particular, if the distribution function  $f(\mathbf{v})$  is determined on the grid  $(v_i, \theta_j, \phi_k)$  then

$$F(v_i) = \frac{1}{\Delta v_i} \sum_{jk} f(v_i, \theta_j, \phi_k) \Delta V_{ijk}$$

The grid was built with a constant density of ions in each spherical shell. The density is determined solely by the number of samples in each shell, the thickness of the shell and the radius to the middle of the shell boundaries. We also required that on the equator  $\Delta \theta = \Delta \phi$ . A full derivation can be found in the appendix.

The final step is to establish the relation between  $\mathbf{v}_0$  and  $\mathbf{v}$ . The model shock profile consists of the uniform upstream and down and the inhomogeneous transition layer. In order to increase the computation efficiency we trace the ions numerically within the transition layer but use the analytical expressions for the trajectories in both uniform regions. Details about

### Initial conditions distribution in phase space.

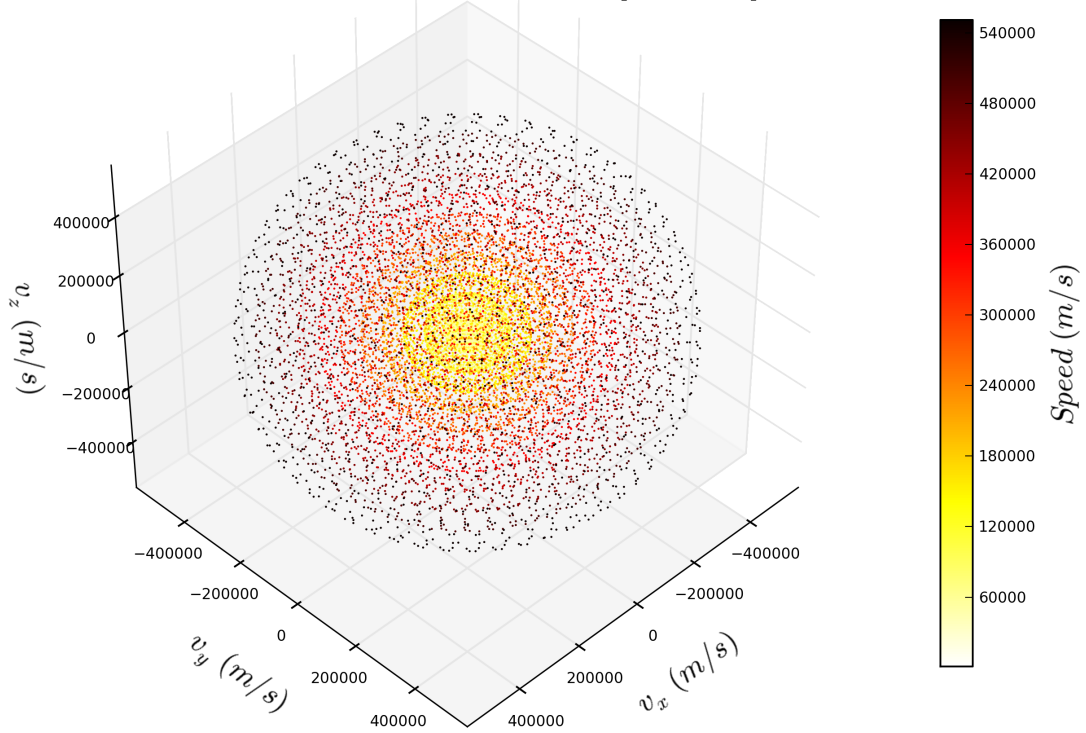


**Figure 3.1:** Velocity spectrum divided into spherical elements. Each point in the graph is a center of a velocity element.

the method that has been used to find the roots of equations of motions are included in appendix C.

To solve the ions equations of motions in the shock transition we use Runge-Kutta scheme

of 4th order for velocity dependent forces [50].

$$\begin{aligned}
\vec{b}_1 &= \vec{y} \left[ \vec{y}_n, \dot{\vec{y}}_n \right] \\
\vec{b}_2 &= \vec{y} \left[ \vec{y}_n + \dot{\vec{y}}_n \frac{\Delta t}{2} + b_1 \frac{(\Delta t)^2}{8}, \dot{\vec{y}}_n + b_1 \frac{\Delta t}{2} \right] \\
\vec{b}_3 &= \vec{y} \left[ \vec{y}_n + \dot{\vec{y}}_n \frac{\Delta t}{2} + b_1 \frac{(\Delta t)^2}{8}, \dot{\vec{y}}_n + b_2 \frac{\Delta t}{2} \right] \\
\vec{b}_4 &= \vec{y} \left[ \vec{y}_n + \dot{\vec{y}}_n \Delta t + b_3 \frac{(\Delta t)^2}{8}, \dot{\vec{y}}_n + b_3 \Delta t \right] \\
\dot{\vec{y}}_{n+1} &= \dot{\vec{y}}_n + \frac{\Delta t}{6} \left[ \vec{b}_1 + 2\vec{b}_2 + 2\vec{b}_3 + \vec{b}_4 \right] + O [(\Delta t)^5] \\
\vec{y}_{n+1} &= \vec{y}_n + \dot{\vec{y}}_n \Delta t + \frac{(\Delta t)^2}{6} \left[ \vec{b}_1 + \vec{b}_2 + \vec{b}_3 \right] + O [(\Delta t)^5]
\end{aligned} \tag{3.2}$$

This task is extremely computational demanding and time consuming.

The convergence of the numerical calculations were checked in two manners:

1. Trajectories of particles, that arrived from the upstream, with the highest energy at the downstream were evaluated and compared for different time steps lengths to ensure their accuracy.
2. The velocity distribution at certain point at the downstream was evaluated and compared for different downstream test particles density. This check is sensitive to the upstream velocity distribution that was chosen.

# Chapter 4

## The solar wind missing energy paradox

Using the numerical method described in the last chapter, we intent to examine the effect of the dissipation mechanism on physical quantities that characterizes shocks. The electrons contribution to the process is modest and we shall focus only with the proton population. The evaluated quantities will be validate using V2 measurements and RH equation.

In order to use the method we must first determine the upstream velocity distribution function. Observations by V2 show, simallry to planetary shocks such as Earth's bow shock [2, 47], that in the TS the SW ions velocity distribution is a Maxwellian [41]. The fitted convected isotropic Maxwell-Boltzmann distribution function is:

$$f(\mathbf{V}) = n_0 \left(\pi \frac{2}{3} V_t^2\right)^{-3/2} \exp \left[ -\frac{(V_x - V_{x0})^2 + (V_y - V_{y0})^2 + (V_z - V_{z0})^2}{\frac{2}{3} V_t^2} \right] \quad (4.1)$$

where  $n_0$ ,  $V_t$ ,  $\mathbf{V}_0$  are  $1300 \text{ (} m^{-3} \text{)}$ ,  $8250 \text{ (} m/s \text{)}$ ,  $(321209, 0, 0) \text{ (} m/s \text{)}$  respectively. The ions density and SW velocity are based on means calculated by Li. et al (2008), using velocity-magnetic field coplanarity and the temperature was taken from MIT Plasma Group data (Published in their website).

As stated already in a previous section, in the spacecraft frame 99.1% of the SW flow is along the shock normal, meaning that we are almost in the NIF. Transforming to NIF raises technical difficulties which lie in the fact that some quantities, such as the PUI velocities, have only their magnitude measured. Our equations of motions and electromagnetic fields fitted functions were developed for a NIF and for keeping consistency we rotate the SW velocity to the shock normal direction. This adds an insignificant inaccuracy, much less than the SW velocity standard deviation, which does not change the reliability of our results.

For a SW distribution injected 1.7 gyroradii ahead of the shock foot, the downstream velocity distribution is plotted in figure 4.1. The velocity phase space projections immediately after the overshoot are plotted in figure 4.2. Several features of figure 4.1 are noteworthy. The distribution changes along the shock normal in periodic cycles of a 2 gyroradii, which happens due to the spinning of the phase space by the magnetic field. This implies that even if the SW was stationary, fluctuations in physical quantities that depend on the distribution would occur along the shock normal.

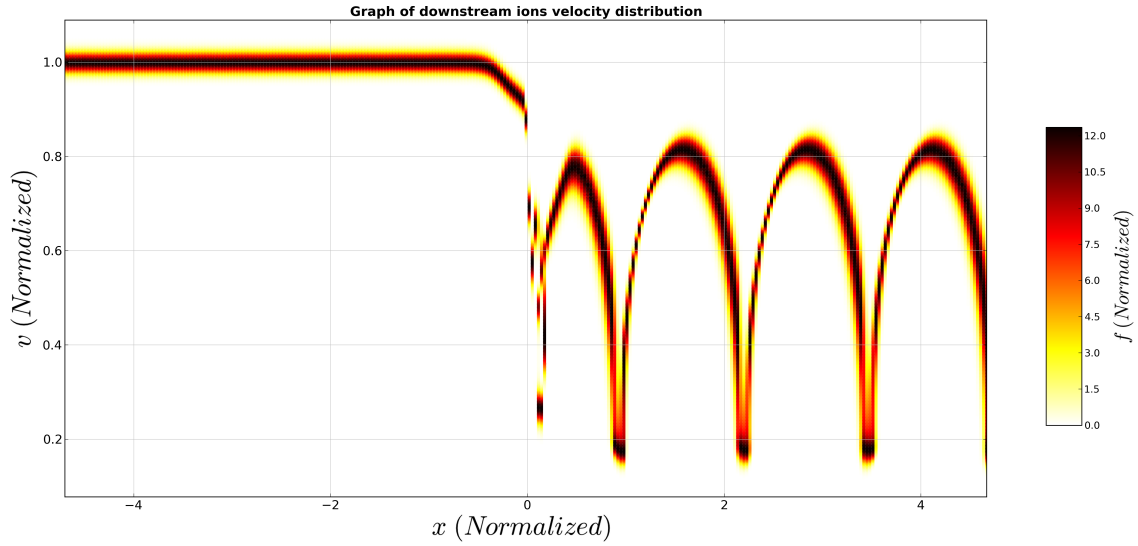


**Figure 4.1:** A plot of downstream ions velocity distribution along the shock normal. The displacement, velocity and distribution are normalized by ions gyroradius, SW flow speed, upstream SW density, respectively.

The downstream phasespace is the figure below is shown to be anisotropic with spread regions of multiply reflected ions in the vicinity of the a decelerated ions.

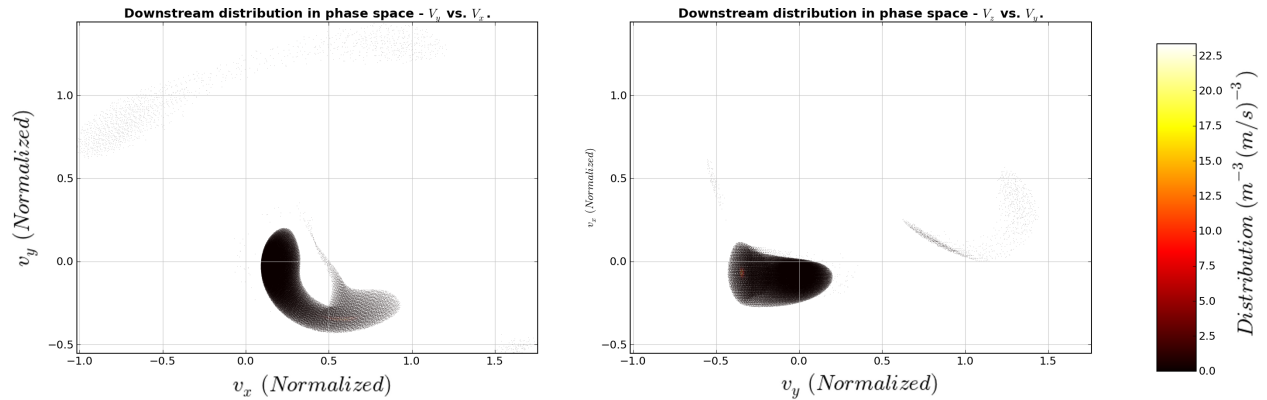


**Figure 4.2:** A plot of a the downstream phasespace projection on the x-y plane and the y-z just after the shock overshoot for the SW distribution. The velocities are normalized by the SW flow speed.

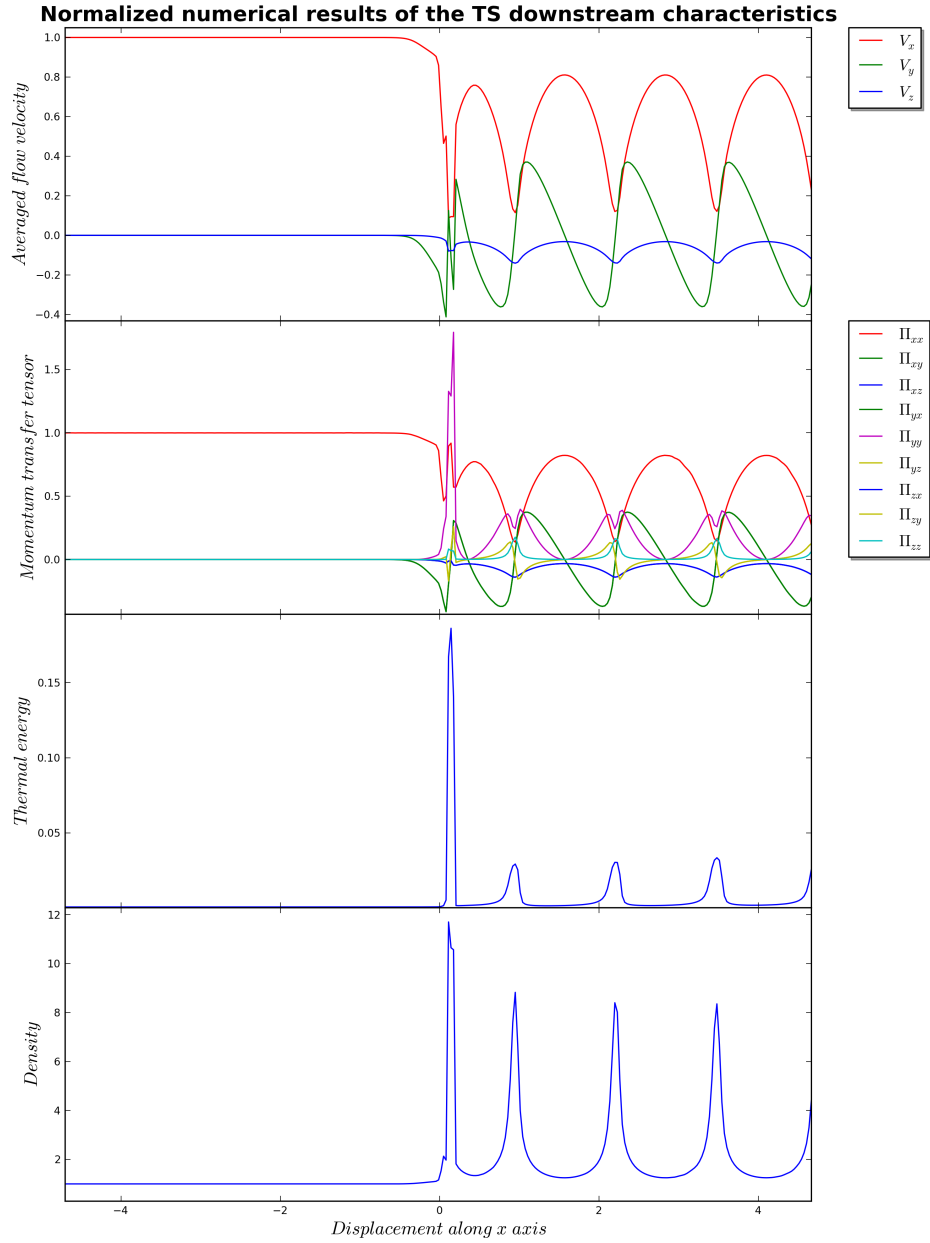


**Figure 4.3:** A plot of SW flow velocity, momentum transfer tensor, thermal energy and density along the shock normal. The Thermal is normalized by the SW kinetic energy. The momentum tensor components are normalized by their  $xx$  component at the upstream for the SW distribution. The rest of the quantities are normalized by their SW upstream value.

In the figure above quantities that appear in the RH relation for momentum conservation are plotted versus the displacement. Its worth noticing that the similarity between the normalized velocity components and the normalized diagonal elements of the momentum transfer tensor is caused by the low plasma temperature, small velocity standard deviation. This indicates that electromagnetic field did not significantly spread out the ions distribution functions, and that the kinetic temperature of the distribution is low.

In the next table we compare between measurements of V2 and the numeric calculation. The observation values of density and SW velocity are means taken over 2.6 hours from the TS cross in which the V2 advanced 3.9 gyroradii [Li et al. 2008]. The observation value of temperature was achieved from MIT Plasma Group data (Published in their website). In order to compare observations to the numeric calculation, the observed velocity was rotated to NIF, means and standard deviation of numeric quantities were taken over a distance of 3 gyroradii along the shock normal.

Quantity	Observation		Calculation	
	Mean	Standard Deviation	Mean	Standard Deviation
Velocity ( $km/s$ )	(170.43, -2.92, 2.40)	(24.09, -3.00, 24.20)	(185.05, 1.74, -21.17)	(72.23, 80.14, 11.12)
Thermal Energy ( $J$ )	$5.69 \cdot 10^{-20}$	$1.69 \cdot 10^{-22}$	$8.23 \cdot 10^{-19}$	$2.20 \cdot 10^{-18}$
Density ( $m^{-3}$ )	2200	1200	3212	2798

**Table 4.1:** Comparison between measurements of V2 and the numeric calculation.

Although there is a difference of an order of magnitude between the observed and calculated thermal energy, both values are very low compared to the SW energy and can not hold the shock dissipated energy.

We state here the mean values with their corresponding standard deviation of the momentum transfer tensor, calculated numerically in units of  $fN/m^2$  (f stands for Femto, a prefix

denoting a factor of  $10^{-15}$ ).

$$\mathbf{\Pi} = \begin{pmatrix} 136.27 & 1.79 & -14.45 \\ 1.79 & 41.99 & 0.22 \\ -14.45 & 0.22 & 5.17 \end{pmatrix} \quad \mathbf{\Pi}_{\text{SD}} = \begin{pmatrix} 45.95 & 57.98 & 7.37 \\ 57.98 & 53.35 & 14.62 \\ 7.37 & 14.62 & 8.92 \end{pmatrix} \quad (4.2)$$

Since distribution is not gyrotropic,  $\langle v_i v_j \rangle \neq 0$  when  $i \neq j$ , the ions gyration phases are not random and hence correlated.

The pressure tensor was found to be anisotropic, the pressure along the z direction ( $P_{zz}$ ) is smaller in one magnitude from the pressure in the x and y directions ( $P_{zz}$  &  $P_{yy}$ ). Hence, immediately downstream we can not express the diagonal components of the transfer momentum tensor in terms of thermal energy and kinetic energy density tensor.

The momentum transfer vector,

$$[\Pi_{1k} + \frac{B^2}{2\mu_0}\delta_{1k} - \frac{B_1 B_k}{\mu_0}] = 0 \quad (4.3)$$

(also defined in the introduction section), was calculated using the displacement averaged quantities. Since the RH relation for momentum density conservation is linear to the momentum transfer tensor it holds also for its displacement average. While in the upstream the momentum transfer vector is  $(225.03, 0.00, 0.66) fJ/m^3$ , downstream it is  $(140.99, 1.79, -13.59) fJ/m^3$ .

The RH jump conditions instruct that these quantities must be conserved. Since there is a large difference between momentum transfer vector at the shock boundaries, the SW alone cannot support the shock. This result is backed up by the observations which implies that ions with energies outside the range of, PLS observation spectrum,  $10 - 5950eV$  have a significant contribution to the total energy density. It is believed that another population of energetic particles, that belong to the spectrum range of  $6 - 10keV$ , gain the missing energy

density via the shock surfing [51, 7, 57, 55]. In the next section the PUI will be considered as candidate for filling the gap between the energy density at the boundaries.

# Chapter 5

## Examination of the pickup ions as a possible solution

A surprising observation was made by V2 when it crossed the TS during the days 242-244 of year 2007. As expected the SW undergoes a transition from supersonic to subsonic flow at the TS. However, the observed increment in SW thermal energy was only up to 4% of the SW dissipated energy [42, 41]. This indicates that the incident SW kinetic energy had to be transferred to some other particle population, possibly PUIs. Comparison of the momentum flux between the shock two sides, that was made in the last section, ratify it.

The shock drift acceleration is known as an energization mechanism of PUI [1, 52]. PUI were shown by test particle approach to be accelerated in TS to high energies by multiply reflections [7]. This makes the PUI a good candidate to be the second particles group that participant in the dissipation process. In this section, the fulfilment of RH equation for momentum conservation by the PUI distribution will be examined.

Since the actual PUI distribution in the TS upstream is not known precisely, a simplified

form of PUI distribution, filled-shell centred at SW flow velocity, is used. It was derived theoretically [49] and verified by SWICS and HISCALE observations near heliospheric shocks by observing  $He^+$  and  $He^{++}$  ions [18].

$$f_{upstream}(v) = A_0(1 - H(v - u)) \left(\frac{v}{u}\right)^{-1.5} \exp\left(-\left(\frac{v}{u}\right)^{-1.5}\right) \quad (5.1)$$

Where  $v$ ,  $u$  and  $A_0$  are the particle velocity, SW upstream flow speed and some constant with units of density per speed, respectively. The value of the spectral index is  $-1.5$ . The value of the amplitude,  $A_0$  is  $2.187 \times 10^{-15} [m^{-3}/(m/s)]$  and was determined by the requirement that the RH relation for momentum conservation is kept.

For a PUI distribution injected 1.7 gyroradii ahead of the shock foot, the downstream velocity distribution is plotted in the figure below.

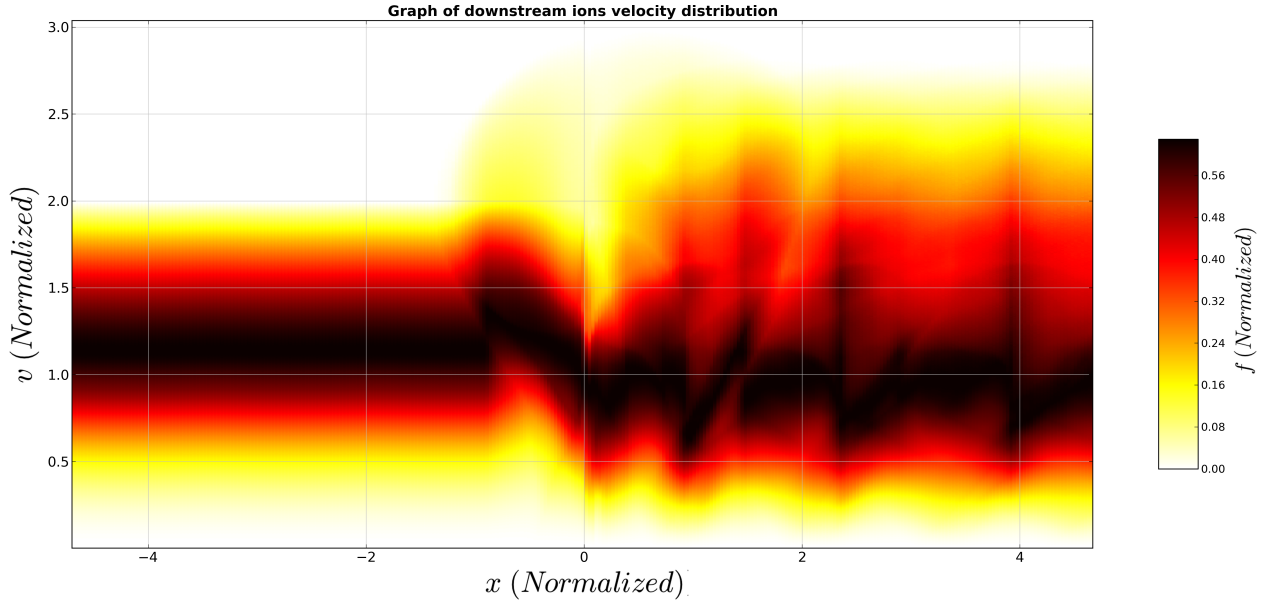


**Figure 5.1:** Plot of downstream PUI velocity distribution along the shock normal. The distribution bar is logarithmic scaled. The displacement, velocity and distribution are normalized by ions gyroradius, SW flow speed, upstream SW density, respectively.

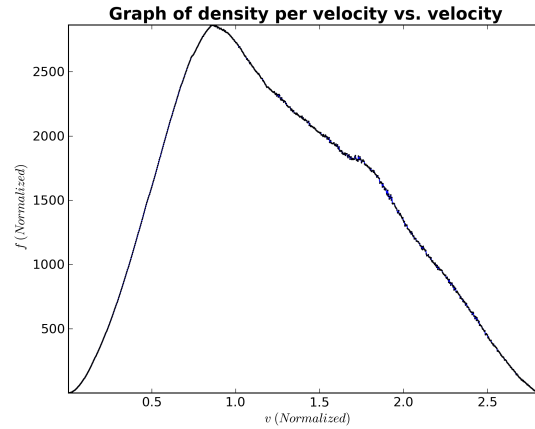


**Figure 5.2:** Plot of downstream PUI velocity distribution at 4.325 gyroradii from the ramp. The displacement, velocity and distribution are normalized by ions gyroradius, SW flow speed, upstream SW density, respectively.

The phasespace just after the shock overshoot is plotted below

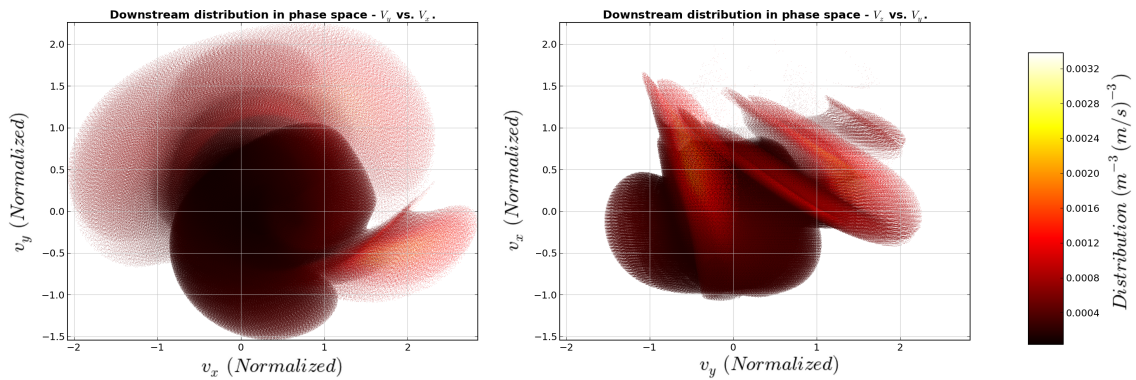


**Figure 5.3:** A Plot of the downstream phasespace projection on the x-y plane and the y-z just after the shock overshoot, 0.7 gyroradii from the ramp, for PUI distribution. The velocities are normalized by the upstream SW flow speed.

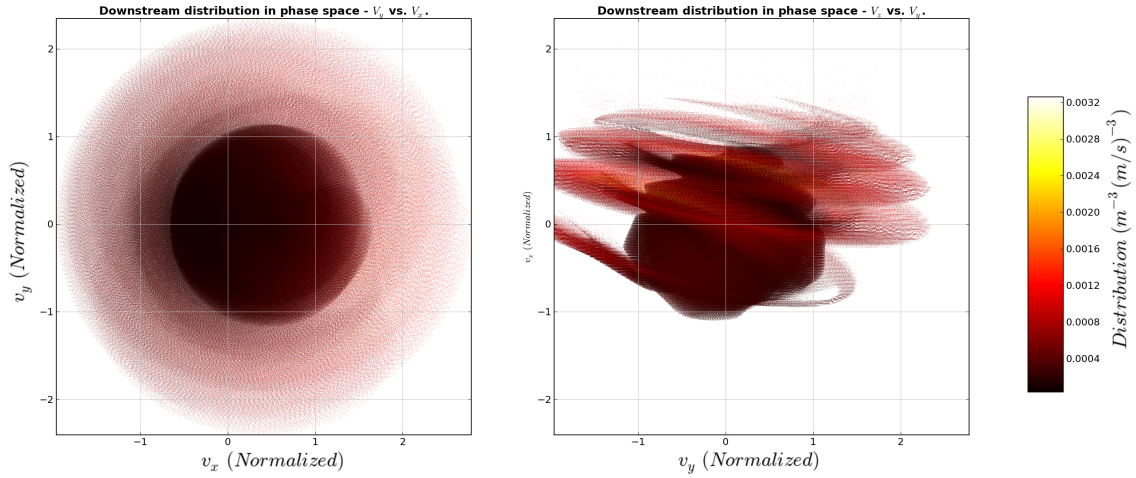


**Figure 5.4:** A Plot of the downstream phasespace projection on the x-y plane and the y-z just after the shock overshoot, 4.435 gyroradii from the ramp, for PUI distribution. The velocities are normalized by the upstream SW flow speed.

The downstream phasespace is shown to be anisotropic, although the y-z projection gets a circular shape after about 4 gyroradii from the ramp. In the figure below quantities that appear in the RH relation for momentum conservation are plotted versus the displacement.

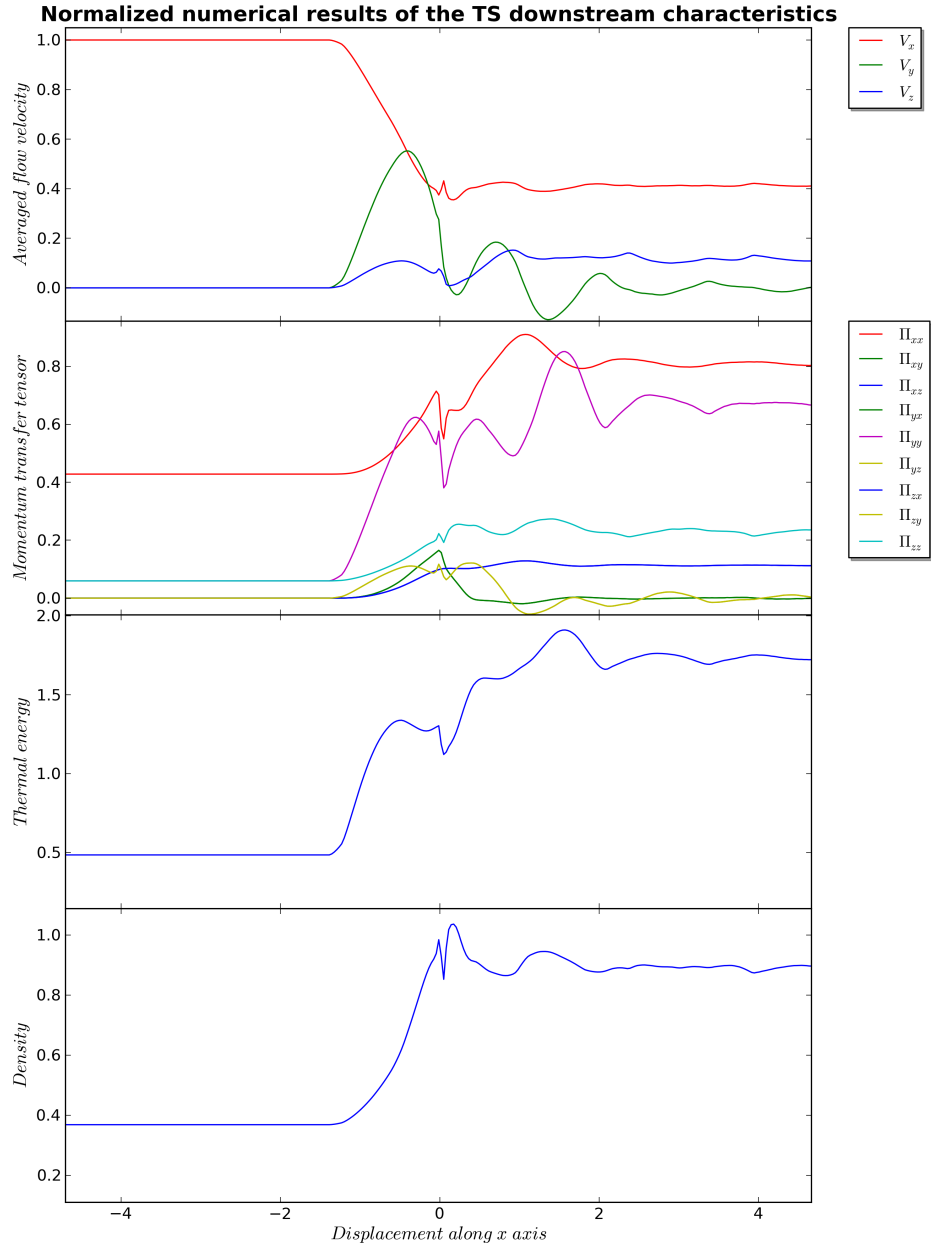


**Figure 5.5:** A Plot of PUI flow velocity, momentum transfer tensor, thermal energy and density along the shock normal. The thermal energy is normalized by the SW kinetic energy. The momentum tensor components are normalized by their  $xx$  component at the upstream for the SW distribution. The rest of the quantities are normalized by their SW upstream value.

Quantities	Upstream		Downstream	
	Mean	Standard Deviation	Mean	Standard Deviation
Velocity ( <i>km/s</i> )	(314.87, 10.64, 2.46)	(18.41, 30.25, 68.84)	(131.19, 3.48, 35.70)	(4.38, 22.83, 9.55)
Thermal Energy ( <i>J</i> )	$4.75 \cdot 10^{-17}$	$1.54 \cdot 10^{-17}$	$1.46 \cdot 10^{-16}$	$1.14 \cdot 10^{-17}$
Density ( $m^{-3}$ )	490	35.40	1173.65	41.93

**Table 5.1:** Means and standard deviations of numeric quantities.

The distribution is almost gyrotropic,  $\langle v_i v_j \rangle \simeq 0$  when  $i \neq j$ . The off diagonal components of the momentum transfer tensor are smaller than the diagonal ones by atleast an order of magnitude. Thus, ions gyration phases are not fully correlated. The pressure tensor was found to be almost isotropic, the off diagonal components are atleast one order of magnitude smaller than the diagonal ones. Hence, we can express the diagonal components of the transfer momentum tensor in terms of thermal energy and kinetic energy density tensor -

$$\left[ \frac{1}{3} n E_{th} + n E_k \right] = 0 \quad (5.2)$$

where  $E_{th}$  and  $E_k$  are the thermal and kinetic energies, respectively. Another property worth mentioning is that the temperature and the density are highly correlated.

In the next table quantities that were calculated numerically are collected. These values are means and standard deviation taken over 4 gyroradii ( 3 hours) from the shock front.

We state here the mean values with their corresponding standard deviation of the momentum transfer tensor, calculated numerically in units of  $fN/m^2$  (f stands for Femto, a prefix denoting a factor of  $10^{-15}$ ).

**Upstream:**

$$\mathbf{\Pi} = \begin{pmatrix} 96.65 & 0.30 & 0.21 \\ 0.30 & 19.24 & 1.35 \\ 0.21 & 1.35 & 13.96 \end{pmatrix} \quad \mathbf{\Pi}_{SD} = \begin{pmatrix} 2.00 & 1.01 & 0.73 \\ 1.01 & 17.06 & 3.88 \\ 0.73 & 3.88 & 1.79 \end{pmatrix} \quad (5.3)$$

**Downstream:**

$$\mathbf{\Pi} = \begin{pmatrix} 181.42 & 0.07 & 25.58 \\ 0.07 & 146.35 & 1.68 \\ 25.58 & 1.68 & 53.17 \end{pmatrix} \quad \mathbf{\Pi}_{\text{SD}} = \begin{pmatrix} 12.37 & 3.50 & 1.36 \\ 3.50 & 19.31 & 10.04 \\ 1.36 & 10.04 & 3.64 \end{pmatrix} \quad (5.4)$$

The momentum transfer vector,

$$\left[ \Pi_{1k} + \frac{B^2}{2\mu_0} \delta_{1k} - \frac{B_1 B_k}{\mu_0} \right] = 0 \quad (5.5)$$

(also defined in the introduction section), was calculated using the displacement averaged quantities. Since the RH relation for momentum density conservation is linear to the momentum transfer tensor it holds also for its displacement average. While in the upstream the momentum transfer vector is  $(97.43, 0.29, 0.87) fJ/m^3$ , downstream it is  $(186.14, 0.01, 27.11) fJ/m^3$ . The difference between the two sides is  $(88.72, -0.22, 26.24) fJ/m^3$  while for the SW it is  $(-84.03, 1.79, -13.58) fJ/m^3$ , showing that PUI can gain the missing energy density via shock surfing. This implies that PUI acceleration can be the one of the major dissipation mechanism in the TS.

An exceptional result for the evaluated density should be pointed out. In order that the PUI would be able to contain the missing energy their density upstream must be about 0.4 of the SW upstream density and downstream about 0.3 of the SW downstream density. This result was not entirely unexpected. Wang et al(2008) observed, with STEREO A and B spacecraft, heliosheath energetic neutral atoms (ENA) between June to October 2007. These ENA were produced by charge exchange of suprathermal ions with interstellar neutral atoms. These ENA are remote traces of energetic ion populations in distant regions, as they retain the parent ion's velocity in the charge exchange process. It was shown that, if the ENA parent heliosheath ions come from the energization of the population by the TS, their spectrum should extend down to the SW energies [51].

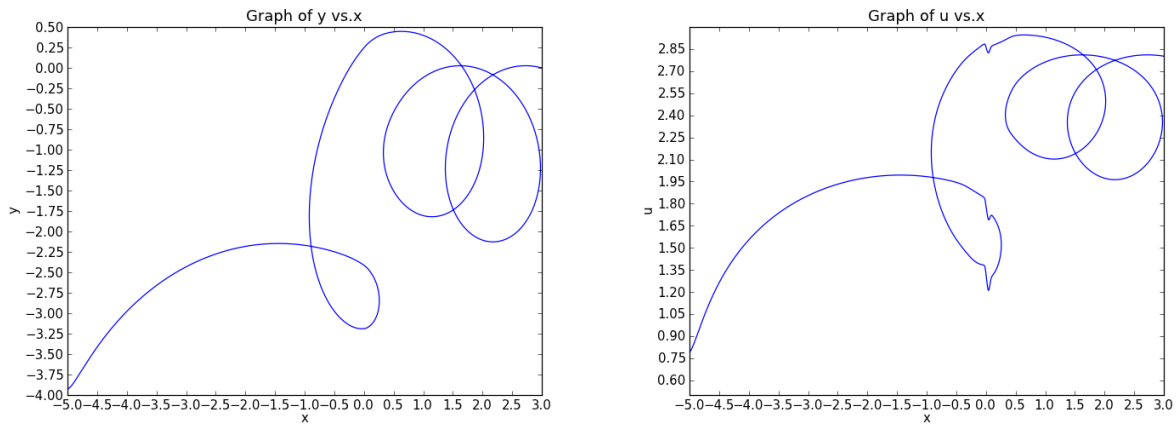


**Figure 5.6:** A ramp drift acceleration (RDA) trajectory which occur frequently. This is a special case of SDA in which the ion is turned around at ramp. The dimensionless displacement axes are normalized by the ion upstream gyroradius and the velocity axis by the SW upstream speed.

# Chapter 6

## An open question - the long tail observed by V2's LECP instrument

The V2 is equipped with an LECP instrument that measures ions density per energy in an energy spectrum of 0.028-3.5 MeV using eight energy-bands.

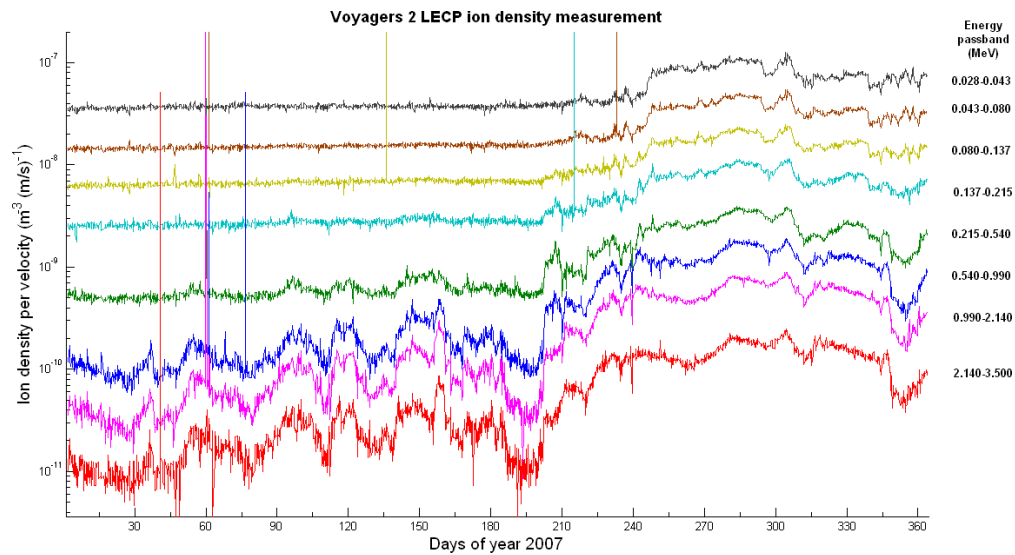


**Figure 6.1:** Daily average of the ion density per velocity in eight Voyager 2 ion channels using good sectors average (1,2,3,5,6,7) calculated with proton energy passbands and efficiencies.

Because telemetry issues, Unfortunately, the observations are not continuous. The parameters of a fitted power law near the third cross of the TS by V2 are given in the figure below.

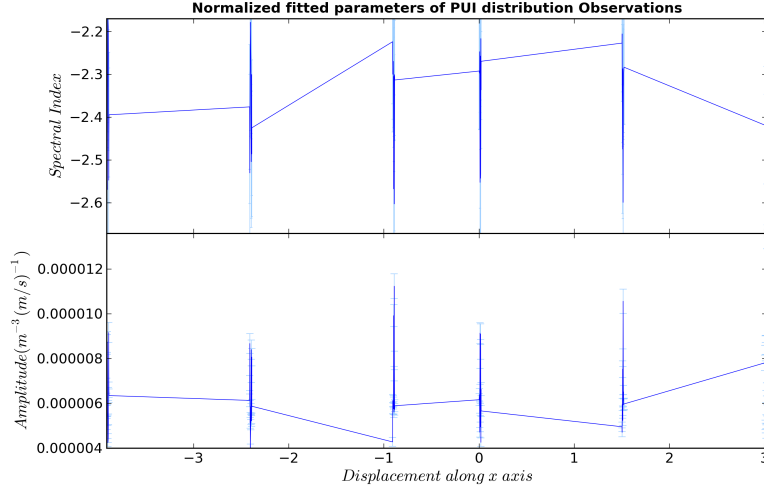


**Figure 6.2:** The fitted parameters, of a power law distribution, for the V2 observed PUI tail (280 - 3500 keV) along the shock normal. The a axis is normalized by the SW upstream gyroradius.

The averaged spectral index and amplitude at distance of about  $-2.4$  gyroradii from the shock ramp is  $-2.355 \pm 0.145$  and  $5.932 \times 10^{-6} \pm 2.783 \times 10^{-7} m^{-3}(m/s)^{-1}$ , respectively. At distance of about  $1.5$  gyroradii spectral index and amplitude are  $-2.334 \pm 0.139$  and  $6.062 \times 10^{-6} \pm 2.708 \times 10^{-7} m^{-3}(m/s)^{-1}$ , respectively. Hence, no significant variations in the immediate region of the shock was observed for energies of 0.028-3.5 MeV. The upstream and downstream particle density in the energy range of 0.0280-3.500 MeV is  $0.11 m^{-3}$  which is %0.01 of SW upstream density. Assuming isotropic momentum transfer tensor, the diagonal elements at the upstream is  $2.51 fJ/m^3$  which is %1.12 of the SW momentum transfer tensor  $xx$  component. Thus, this tail cannot be the answer for the dissipation question.

This tail was not observed in the numerical calculation. In order to exclude the possibility of insufficient test particles per energy shell we compared the density of PUI with velocity

of  $10^6 \pm 10^3$   $m/s$  at 1.7 gyroradii after the ramp for various number of the test particles ( $10^4 - 10^6$ ). Various time step were also checked (600 - 1000 steps per SW ion gyration time,  $\Omega_u^{-1}$ ). No PUI in the energy range specified above were found during the examination.

As shown in the section about the TS electromagnetic fields, the shock ramp at V2 third cross was found to be serrated.

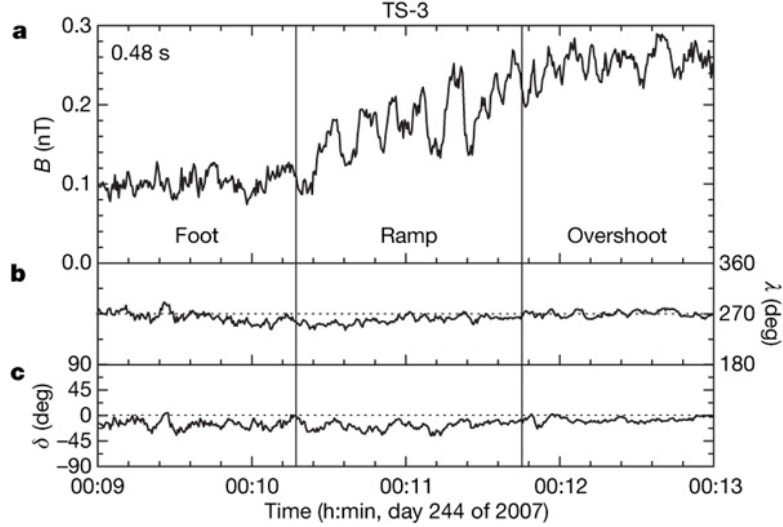


**Figure 6.3:** The structure is based on observations of the magnetic field strength  $B$  (a) and its directions  $\lambda$  (b) and  $\delta$  (c) at 0.48-s intervals (Here the directions lambda and delta of  $B$  are in heliographic coordinates.). The magnetometer on Voyager 2 sampled the vector magnetic fields in the termination shock at a rate of 2.08 samples s<sup>-1</sup>, and the spacecraft was able to transmit all of this information, making it possible to determine the complex internal structure of the ramp shown here [5].

We added teeth with a similar width and height as observed to the shock ramp profile by adding to the former profile function a series of sinc functions -

$$\sum_n a \operatorname{sinc}(b(x + c_n)) \quad (6.1)$$

where  $a$  and  $b$  are  $6 \cdot 10^{-11}/Bu$  and  $6.9/Dr$ , respectively.  $c_n$  was defined as  $\frac{4-2n}{10}Dr$  with  $0 \leq n \leq 4$ . The serrated profile is built just for introducing qualitative results. The magnetic

and electric field profiles with and without the addition of teeth in ramp are plotted in the figure below.

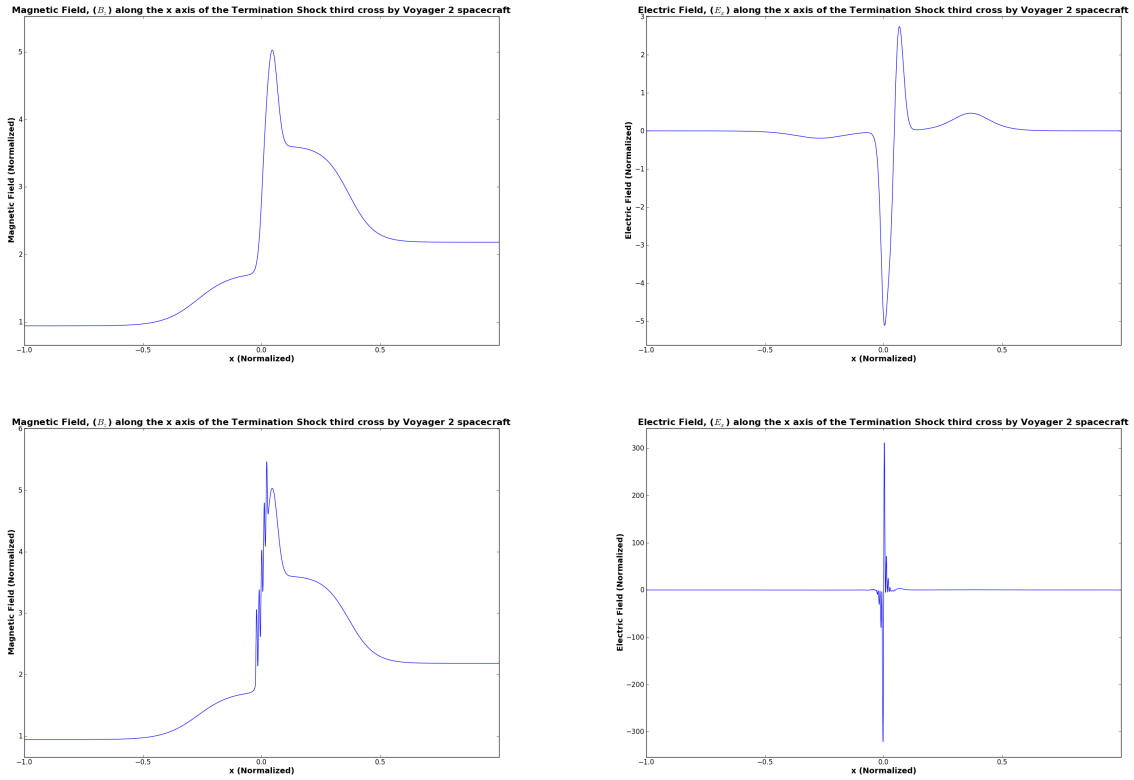


**Figure 6.4:** Plots of the magnetic (right) and electric (left) field profiles without (upper) and with (bottom) the addition of teeth in ramp.

The two PUI velocity distribution, corresponding to the two profiles introduced above, are plotted at 20 gyroradii from the shock ramp in the figure below.

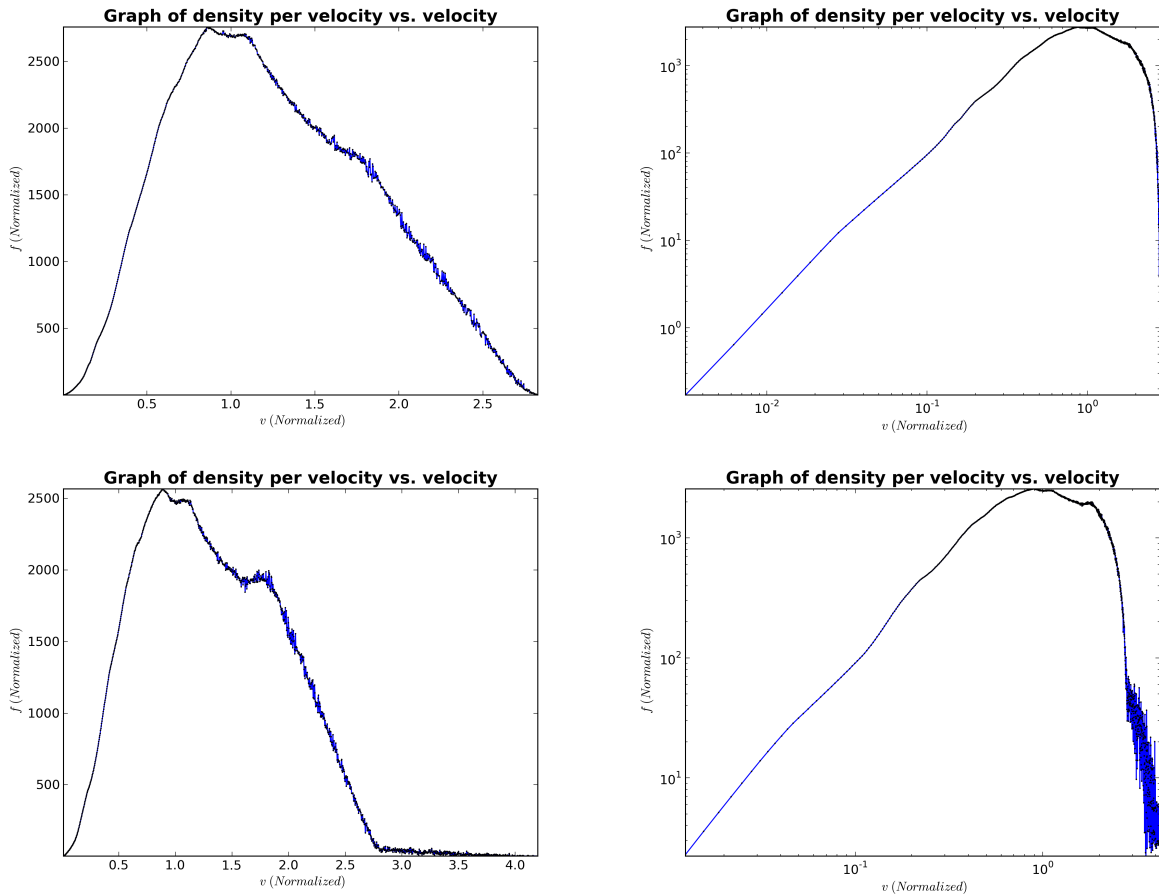


**Figure 6.5:** Plots of ions velocity distribution for smooth ramp (top) and serrated ramp (bottom) with a linear scaled axes (left) and logarithmic scaled axes (bottom). The dimensionless displacement axis is normalized by the ion upstream gyroradius, the velocity axis by the SW upstream speed and the density by the SW upstream density.

By adding teeth to the ramp, a long tail appeared in the distribution. Since the PUI density in the tail is much smaller compared to rest of the distribution, its contribution the momentum transfer tensor is small, an addition of about % 12 to the xx component, and the results derived earlier hold.

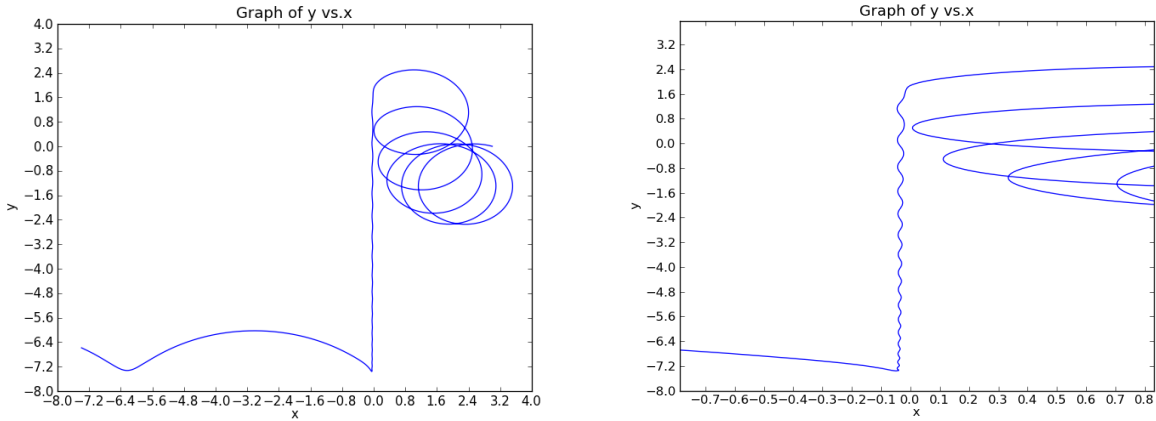


**Figure 6.6:** Example of an ion trajectory gaining high-energy by SDA through the TS serrated profile. The right-hand panel gives close-up of the shock surfing along fluctuations in the ramp. The displacement is normalized by the upstream gyroradii.

Although adding fluctuations to the ramp increased the maximum energy that PUI can gain, the maximum energy was only 10 times bigger than the SW energy (i.e. about 5KeV) while the measured tail was up to 7000 times bigger (i.e about 3.5 MeV). The reason might be that

- The shock normal was not determined correctly and the shock angle might be more than 70 degrees.
- The relative speed between the V2 and the TS was different than assumed and the shock ramp is more narrow.
- The assumed CSP was too low. The dependence of the maximum and average energy that PUI can gain on the two last parameters was considered by Burrows et al. 2010 for the TS with a shock angle of 90 degrees [7].
- The intensity of energetic particles rose exponentially during the 40 days that preceded the V2 encounter with the TS and reached a plateau 7 days after V2 crossed the TS. In addition the SW flow velocity decreased from 380 km/s far upstream to 300 km/s at the shock. Florinski et al. (2009) showed that that the gradual slowdown of the SW during last 40 days of V2 observations in the SW is plausibly explained by the pressure energetic particles exert on the back-ground plasma, based on gas-dynamic conservation laws. They assumed the shock

was stationary and that the diffusion coefficient did not vary along the shock normal. This study shows that First order Fermi acceleration might be the mechanism that is responsible for this energetic population. [15]

# Chapter 7

## Conclusions

We have studied the pickup ion dynamics within the termination shock and their contribution to Rankine-Hugoniot relations - pressure balance or energy-momentum conservation across the shock front. In our analysis we used the magnetic field measured by Voyager 2 at one of the shock crossings when the observations seemed to be of best quality. In contrast with previous works regarding the shock as perpendicular, we analyzed an oblique geometry with the shock angle  $\theta_{Bn} = 70^\circ$ , in accordance with the shock parameters deduced from observations. For the analysis the cross-shock potential was used found from the requirements of low heating of solar wind ions, as measured by Voyager. The study has been done by following ion trajectories back in time followed by Liouville mapping to the upstream distribution which is assumed to be known.

We have found that pickup ions, distributed as a filled shell just upstream of the shock, undergo efficient surfing/multiple reflection energy. The far downstream distribution grows a substantial superthermal energy tail up to 10 times of the solar wind proton energy. The energy spectrum did not follow a power-law. The acceleration has been studied for the shock profile with and without fine structure. The fine structure consists of a series of "teeth" and

was suggested earlier to be a part of the stationary shock structure, at least at the times scales significantly exceeding the typical acceleration time. We have found that the fine structure is responsible for the growth of the high energy tail well beyond the 10 incident proton energies.

We found, in a good agreement with observations, that the downstream distribution of the accelerated PUIs consists of the moderate energy part with a rather gradual power-law spectrum and a higher energy part which is steeper. The transition from moderate to high energies is accompanied by a substantial drop in the distribution function, so that the contribution of the high-energy part into the overall plasma pressure remains small, relative to the other part. We found that the PUI pressure (dynamic and kinetic altogether) increases by a factor of about two from upstream to downstream. The latter means that, in order to provide necessary contribution into Rankine-Hugoniot relations and maintain the shock stationary, the upstream PUI density should be sufficiently high, so that their pressure be compatible, up to 40%, to the solar wind pressure. If this is the case, the shock is a high-beta shock with a rather peculiar upstream distribution. Shocks of this kind have not been treated analytically so far and probably a revision of existing models is required.

Observations by V2 shown a high energy power law spectrum (0.028-3.5 MeV). The intensity of the most energetic ions started to increase about 775 gyroradius before the TS. This was accompanied with a decrement of the SW flow speed from about 380 km/s to about 300 km/s, which began far upstream and ended at the TS. This observation could not be explained by our deterministic test particle approach which accelerated particles only up to 3.9 KeV, nor the SW speed decrement which began only about 1.7 gyroradius before the shock. Florinski et al. (2008) found from observations that the average diffusion coefficient for energetic particles (1-3.5 MeV) was  $10^{16}(m^2 s^{-1})$ . They showed that the precursor of the quantities mentioned above can be explained by First order Fermi acceleration [15]. The length scale of the slowdown is the diffusive length ( $D/U$ , where  $D$  is the momentum-averaged value of the

radial diffusion coefficient and  $U$  is the flow speed). The radial diffusion length scale is 473 gyroradius, which entails that the diffusion effects are irrelevant for SDA. The contribution of the energetic particles (0.028-3.5 MeV) to the momentum transfer tensor is about %1.1 of the SW momentum transfer tensor  $xx$  component and can not explain the dissipation process.

# Appendix A

## The equations of motion in the TS boundaries

In the TS normal incidence frame (a rest frame of the shock moving along the front such that the inflow is normal to the front), which is assumed to be stationary and homogeneous, we have an oblique discontinuity ( $B_n \neq 0$ ,  $\rho_{u,d}\mathbf{U}_{u,d} \cdot \mathbf{n} \neq 0$ ) chosen such that it lays at  $x = 0$  so the fluid velocity is  $(U_u, 0, 0)$  relative to the shock front[Richardson et al.2008]. The equations of motion for a test particle (Lorentz equations) in this frame work given in SI units:

$$m_i \dot{v}_x = eE_x + e(v_y B_z - v_z B_y) \tag{A.1}$$

$$m_i \dot{v}_y = eE_y + e(v_z B_x - v_x B_z) \tag{A.2}$$

$$m_i \dot{v}_z = eE_z + e(v_x B_y - v_y B_x) \tag{A.3}$$

The fields are chosen in a non self-consistent way. We assume that far from the TS we have ideal MHD (isotropic pressure, no heat flux nor electrical resistivity) and that the variation close to it is small but non neglectable. We relate the field in each side of the TS with the RH relations (Rankine Hugoniot relations). However, these relations appropriate only for

isotropic pressure so we need to adjust the fields to make them suitable to describe the fields near the TS. It is done by keeping the relations that imply equal quantities in both sides and let loose relations of quantities that exhibit a jump.

We choose the front normal and the upstream magnetic field to lie in the x-z plane in such a way that the front normal lies on the x-axis and headed in the same direction. We also take in account that  $U_{un} \neq U_{dn}$  [42, 33]. Solving the following set of equations

$$\textit{Electromagnetic discontinuity relations} \quad [\mathbf{E}_t] = 0, [\mathbf{B}_n] = 0 \quad (\text{A.4})$$

$$\textit{Ideal MHD equation} \quad \mathbf{E} + \mathbf{U} \times \mathbf{B} = 0 \quad (\text{A.5})$$

$$\textit{Coplanarity theorem} \quad (\mathbf{U}_{un} - \mathbf{U}_{dn})(\mathbf{B}_{ut} \times \mathbf{B}_{dt}) = 0 \quad (\text{A.6})$$

we deduce the relations between the upstream and downstream fields:

$$\mathbf{B}_u = B_u(\cos \theta, 0, \sin \theta) \quad (\text{A.7})$$

$$\mathbf{B}_d = B_u(\cos \theta, 0, R \sin \theta) \quad (\text{A.8})$$

$$\mathbf{E}_u = \mathbf{E}_d = (0, U_u B_u \sin \theta, 0) \quad (\text{A.9})$$

where  $\mathbf{v}$  denotes test particle velocity,  $\mathbf{E}$  denotes electric field,  $\mathbf{B}$  denotes magnetic field,  $\mathbf{n}$  denotes the shock normal,  $\mathbf{R}$  denotes compression ratio,  $\theta$  denotes angle between the shock normal and magnetic field,  $m_i$  denotes ion mass and  $e$  denotes electron charge. We proceed with rewriting the equations of motion in dimensionless form as follows:

$$\dot{u}_x = u_y b_z \quad (\text{A.10})$$

$$\dot{u}_y = e_y + u_z b_x - u_x b_z \quad (\text{A.11})$$

$$\dot{u}_z = -u_y b_x \quad (\text{A.12})$$

where  $\mathbf{u} \equiv \frac{\mathbf{v}}{U_u}$ ,  $\mathbf{b} \equiv \frac{\mathbf{B}}{B_u}$ ,  $\tau \equiv \Omega_u t$ ,  $\Omega_u = \frac{eB_u}{m_i}$ ,  $e_y = \frac{E_y}{U_u B_u} = \sin \theta$  and  $U_u$  denotes the upstream plasma velocity (solar wind). Solving this ordinary differential equations set using Fundamental Matrices Method we find:

$$u_x = \frac{1}{b_x^2 + b_z^2} \left[ e_y b_z + u_{x0} b_x^2 + u_{z0} b_x b_z - (b_z e_y - u_{x0} b_z^2 + u_{z0} b_x b_z) \cos(\sqrt{b_x^2 + b_z^2} \tau) + u_{y0} b_z \sqrt{b_x^2 + b_z^2} \sin(\sqrt{b_x^2 + b_z^2} \tau) \right] \quad (\text{A.13})$$

$$u_y = \frac{1}{b_x^2 + b_z^2} \left[ u_{y0} (b_x^2 + b_z^2) \cos(\sqrt{b_x^2 + b_z^2} \tau) + \sqrt{b_x^2 + b_z^2} (e_y + u_{z0} b_x - u_{x0} b_z) \sin(\sqrt{b_x^2 + b_z^2} \tau) \right] \quad (\text{A.14})$$

$$u_z = \frac{1}{b_x^2 + b_z^2} \left[ -e_y b_x + u_{x0} b_x b_z + u_{z0} b_z^2 + (b_x e_y - u_{x0} b_x b_z + u_{z0} b_z^2) \cos(\sqrt{b_x^2 + b_z^2} \tau) - u_{y0} b_x \sqrt{b_x^2 + b_z^2} \sin(\sqrt{b_x^2 + b_z^2} \tau) \right] \quad (\text{A.15})$$

Rewriting the equations above in a more convenient form yields:

$$u_x = V_x + SV_{\perp} \cos(\omega\tau - \alpha) \quad (\text{A.16})$$

$$u_y = -SV_{\perp} \frac{\omega}{b_z} \sin(\omega\tau - \alpha) \quad (\text{A.17})$$

$$u_z = V_z - SV_{\perp} \frac{b_x}{b_z} \cos(\omega\tau - \alpha) \quad (\text{A.18})$$

where

$$V_x = \frac{e_y b_z + u_{x0} b_x^2 + u_{z0} b_x b_z}{b_x^2 + b_z^2} \quad (\text{A.19})$$

$$V_z = \frac{-e_y b_x + u_{x0} b_x b_z + u_{z0} b_z^2}{b_x^2 + b_z^2} \quad (\text{A.20})$$

$$V_{\perp} = \frac{\sqrt{(e_y b_z - u_{x0} b_z^2 + u_{z0} b_x b_z)^2 + (u_{y0} b_z \sqrt{b_x^2 + b_z^2})^2}}{b_x^2 + b_z^2} \quad (\text{A.21})$$

$$\omega = \sqrt{b_x^2 + b_z^2} \quad (\text{A.22})$$

$$\alpha = \arctan \left( \frac{u_{y0} \sqrt{b_x^2 + b_z^2}}{u_{x0} b_z - e_y - u_{z0} b_x} \right) \quad (\text{A.23})$$

$$S = \begin{cases} -1 & \text{if } \text{sign}(u_{y0} \sin \theta) = -\text{sign}(\sin \alpha) \\ 1 & \text{if } \text{sign}(u_{y0} \sin \theta) = \text{sign}(\sin \alpha) \end{cases} \quad (\text{A.24})$$

# Appendix B

## Building a three dimensional grid

Here we derive a three dimensional grid in spherical coordinates in the velocity phase space,

$$v_x = v \sin \theta \cos \phi, \quad v_y = v \sin \theta \sin \phi, \quad v_z = v \cos \theta \quad (\text{B.1})$$

The volume of the cell  $(\Delta v, \Delta \theta, \Delta \phi)$  is

$$\begin{aligned} \Delta V &= \int_{R-\frac{\Delta R}{2}}^{R+\frac{\Delta R}{2}} \int_{\theta-\frac{\Delta \theta}{2}}^{\theta+\frac{\Delta \theta}{2}} \int_{\phi-\frac{\Delta \phi}{2}}^{\phi+\frac{\Delta \phi}{2}} r^2 dr \sin \theta d\theta d\phi = \\ &= \frac{\Delta \phi}{3} \left( \left( R + \frac{\Delta R}{2} \right)^3 - \left( R - \frac{\Delta R}{2} \right)^3 \right) \left( \cos \left( \theta - \frac{\Delta \theta}{2} \right) - \cos \left( \theta + \frac{\Delta \theta}{2} \right) \right) = \\ &= \frac{\Delta \phi}{3} \left( 2 \sin \theta \sin \frac{\Delta \theta}{2} \right) \left( 6 R^2 \left( \frac{\Delta R}{2} \right) + 2 \left( \frac{\Delta R}{2} \right)^3 \right) = \\ &= \Delta \phi \sin \theta \sin \frac{\Delta \theta}{2} \left( 2 R^2 \Delta R + \frac{\Delta R^3}{6} \right) \end{aligned} \quad (\text{B.2})$$

We would like to determine the density of ions in each element in a way that relates a single point to each infinitesimal volume center. The ions density that suites this requirement would be

$$\rho = \frac{N}{V} = \frac{1}{\Delta V} \quad (\text{B.3})$$

Now we choose the space between each sampled speed,  $\Delta R$ , and the number of elements in each sample,  $N$ . These parameters determine the density value

$$\rho = \frac{N}{\frac{4}{3}\pi \left( \left( R + \frac{\Delta R}{2} \right)^3 - \left( R - \frac{\Delta R}{2} \right)^3 \right)} = \frac{N}{\frac{4}{3}\pi \left( 6R^2 \left( \frac{\Delta R}{2} \right) + 2 \left( \frac{\Delta R}{2} \right)^3 \right)} \quad (\text{B.4})$$

Hence, a relationship between those two parameters and the element volume may be defined.

Now we use equations 2 and 3 to express  $\Delta\phi$

$$\Delta\phi = \left( \rho \sin\theta \sin\frac{\Delta\theta}{2} \left( 2R^2\Delta R + \frac{\Delta R^3}{6} \right) \right)^{-1} \quad (\text{B.5})$$

where  $\rho$  is provided in equation 4.

$\Delta\theta$  is determined by the requirement that whenever  $\theta = \pi/2$  then  $\Delta\theta = \Delta\phi$ . So it constitutes the solution for the following equation

$$\begin{aligned} \tilde{R} &\equiv 6R^2 \left( \frac{\Delta R}{2} \right) + 2 \left( \frac{\Delta R}{2} \right)^3 \\ \Delta\theta &= \left( \rho \sin\frac{\Delta\theta}{2} \tilde{R} \right)^{-1} \end{aligned} \quad (\text{B.6})$$

To solve this equation we expand  $\sin\frac{\Delta\theta}{2}$  up to the 8th order, which can be solved analytically with use the Ferrari's formula. After expansion, the equation transforms into

$$\frac{X^1}{1!} - \frac{X^2}{3!} + \frac{X^3}{5!} - \frac{X^4}{7!} = \frac{1}{\rho\tilde{R}} \quad \text{where } X \equiv \frac{\Delta\theta^2}{2} \quad (\text{B.7})$$

and we choose the single real positive solution. We may roughly estimate a solution expressed by first order expansion

$$\Delta\theta = \sqrt{\frac{2}{\rho\tilde{R}}} \quad (\text{B.8})$$

Now  $\Delta\theta$  are  $\Delta\phi$  expressed as a function of  $R, \theta, N, \Delta R$ . We end-up with a set of equations (2,4,5 and 8) that are used to distribute points and relate them to velocity elements.

# Appendix C

## The roots of the equations of motions for a test particle in constant fields

In the upstream and down the magnetic field is perpendicular to the electric field. The motion of the ions can therefore be described as a superposition of three different motions. The first one is a parallel motion - a constant velocity along the magnetic field direction. The second one is a drift motion - a constant velocity that is orthogonal to the electric and magnetic fields. The third one is a gyromotion - gyration around the magnetic field axis with constant speed and gyroradius. The equations of motion of the ions in those regions were derived in appendix A. In order to determine whether the ion is heading to the shock transition or rather escape to infinity, the first positive root of the equation of motion along the x axis for both regions must be found. The solution isn't straight forward since the equation of motion is a transcendental equation involving a linear and a sinusoidal part

$$x(t) = A + B \cdot t + C \sin(D \cdot t + E) \quad (\text{C.1})$$

where  $A, B, C, D$  and  $E$  are constants determined in general by the electromagnetic fields and initial conditions (for an extended explanation see appendix A). In order to find the first positive root of the transcendental equation the following method is adopted. The bound-

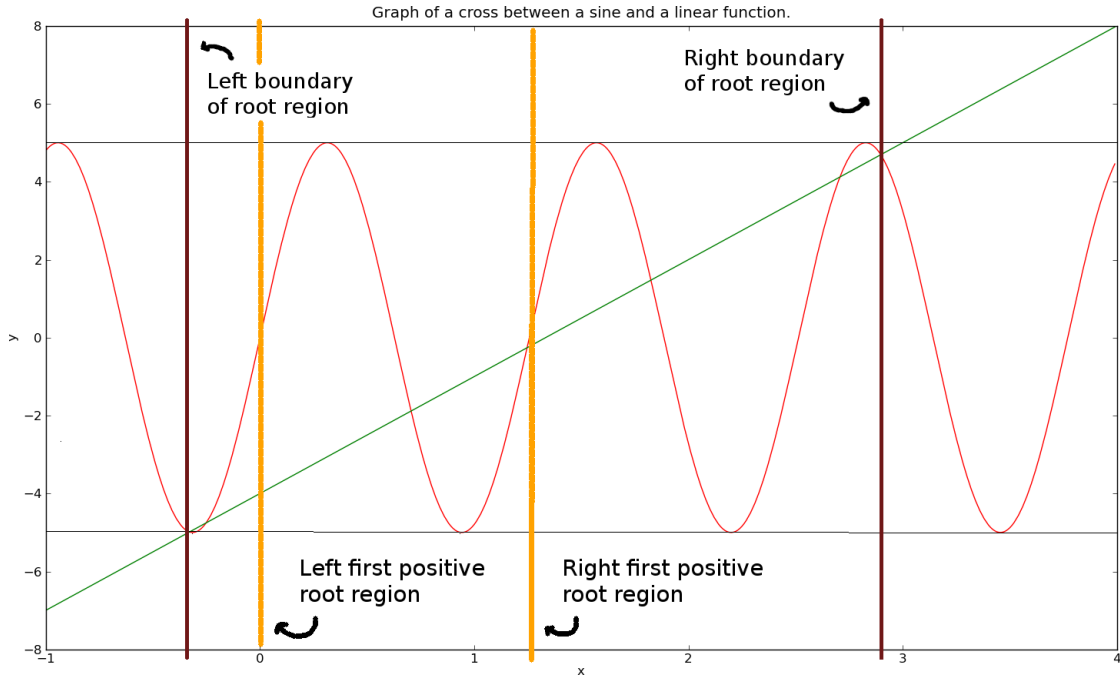


**Figure C.1:** linear and a sinusoidal part of transcendental equation with boundaries of the roots and first positive root regions.

aries of the roots region are set when the linear part crosses the lower and upper amplitude of the sine function. The side of each boundary, linked to a different cross, depends whether the linear part ascends or descends. When a first positive root exists, it is situated in a region bounded to the left at zero, and bounded to the right at  $Max(0, LRR) + \frac{2\pi}{|D|}$  where  $Max(0, LRR)$  is a function that returns the largest value between zero and the left roots region,  $\left( Max(0, LRR) \equiv \frac{|LRR| + LRR}{2} \right)$  and  $D$  is defined above. The first positive root is included inside the cross section of the two regions which are defined above.

For the purpose of finding the root inside the cross section, the sinusoidal part of the equation of motion along the x axis is expanded around the middle of cross section, up to the fourth order. Using Ferrari's formula, we check if any real positive roots lies in the segment. The smallest first real positive root is substituted it in the equation of motion to check its

accuracy. If the root does not meet tolerance limits, the Newton-Raphson method is used to improve the approximation.

# Bibliography

- [1] T. P. Armstrong, M. E. Pesses, and R. B. Decker. Shock drift acceleration. *Washington DC American Geophysical Union Geophysical Monograph Series*, 35:271–285, 1985.
- [2] S. J. Bame, D. J. McComas, B. L. Barraclough, J. L. Phillips, K. J. Sofaly, J. C. Chavez, B. E. Goldstein, and R. K. Sakurai. The ULYSSES solar wind plasma experiment. *Astronomy and Astrophysics, Supplement*, 92:237–265, January 1992.
- [3] K. W. Behannon, M. H. Acuna, L. F. Burlaga, R. P. Lepping, N. F. Ness, and F. M. Neubauer. Magnetic field experiment for Voyagers 1 and 2. *Space Science Reviews*, 21:235–257, December 1977.
- [4] H. S. Bridge, J. W. Belcher, R. J. Butler, A. J. Lazarus, A. M. Mavretic, J. D. Sullivan, G. L. Siscoe, and V. M. Vasyliunas. The plasma experiment on the 1977 Voyager mission. *Space Science Reviews*, 21:259–287, December 1977.
- [5] L. F. Burlaga, N. F. Ness, M. H. Acuña, R. P. Lepping, J. E. P. Connerney, and J. D. Richardson. Magnetic fields at the solar wind termination shock. *Nature*, 454:75–77, July 2008.
- [6] L. F. Burlaga, N. F. Ness, M. H. Acuña, J. D. Richardson, E. Stone, and F. B. McDonald. Observations of the Heliosheath and Solar Wind Near the Termination Shock by Voyager 2. *Astrophysical Journals*, 692:1125–1130, February 2009.

- [7] R. H. Burrows, G. P. Zank, G. M. Webb, L. F. Burlaga, and N. F. Ness. Pickup Ion Dynamics at the Heliospheric Termination Shock Observed by Voyager 2. *Astrophysical Journal*, 715:1109–1116, June 2010.
- [8] R. B. Decker, S. M. Krimigis, E. C. Roelof, M. E. Hill, T. P. Armstrong, G. Gloeckler, D. C. Hamilton, and L. J. Lanzerotti. Mediation of the solar wind termination shock by non-thermal ions. *Nature*, 454:67–70, July 2008.
- [9] W. Droege. Transport of solar energetic particles. *Astrophysical Journals*, 90:567–576, February 1994.
- [10] W. Dröge. Particle Scattering by Magnetic Fields. *Space Science Reviews*, 93:121–151, July 2000.
- [11] W. Dröge. Acceleration and Propagation of Solar Energetic Particles. In L. Klein, editor, *Energy Conversion and Particle Acceleration in the Solar Corona*, volume 612 of *Lecture Notes in Physics*, Berlin Springer Verlag, pages 193–212, 2003.
- [12] L. A. Fisk, G. Gloeckler, and T. H. Zurbuchen. Acceleration of Low-Energy Ions at the Termination Shock of the Solar Wind. *Astrophysical Journal*, 644:631–637, June 2006.
- [13] V. Florinski. Pickup Ion Acceleration at the Termination Shock and in the Heliosheath. *Space Science Reviews*, 143:111–124, March 2009.
- [14] V. Florinski, R. B. Decker, and J. A. le Roux. Pitch angle distributions of energetic particles near the heliospheric termination shock. *Journal of Geophysical Research (Space Physics)*, 113:7103, July 2008.
- [15] V. Florinski, R. B. Decker, J. A. le Roux, and G. P. Zank. An energetic-particle-mediated termination shock observed by Voyager 2. *Journal of Geophysical Research (Space Physics)*, 36:12101, June 2009.

- [16] M. Gedalin. Ion reflection at the shock front revisited. *Journal of Geophysics Research*, 101:4871–4878, March 1996.
- [17] M. Gedalin, M. Liverts, and M. A. Balikhin. Distribution of escaping ions produced by non-specular reflection at the stationary quasi-perpendicular shock front. *Journal of Geophysical Research (Space Physics)*, 113:5101, May 2008.
- [18] G. Gloeckler, L. A. Fisk, and L. J. Lanzerotti. Pickup Ions Upstream and Downstream of Shocks. In G. Li, G. P. Zank, & C. T. Russell, editor, *The Physics of Collisionless Shocks: 4th Annual IGPP International Astrophysics Conference*, volume 781 of *American Institute of Physics Conference Series*, pages 252–260, August 2005.
- [19] G. Gloeckler and J. Geiss. Heliospheric and Interstellar Phenomena Deduced From Pickup ion Observations. *Space Science Reviews*, 97:169–181, May 2001.
- [20] T.I. Gombosi. *Physics of the Space Environment*. Cambridge Atmospheric and Space Science Series. Cambridge University Press, 2004.
- [21] J. T. Gosling. Ion acceleration at shocks in interplanetary space - A brief review of recent observations. *Space Science Reviews*, 34:113–126, February 1983.
- [22] P. A. Isenberg. Evolution of interstellar pickup ions in the solar wind. *Journal of Geophysical Research (Space Physics)*, 92:1067–1073, February 1987.
- [23] J. R. Jokipii, J. Giacalone, and J. Kóta. The physics of particle acceleration at the heliospheric termination shock. *Planetary Space Science*, 55:2267–2272, December 2007.
- [24] M. B. Kallenrode. Acceleration and propagation of energetic charged particles in the inner heliosphere. *Nuclear Physics B Proceedings Supplements*, 39:45–56, February 1995.

- [25] C. F. Kennel, J. P. Edmiston, and T. Hada. A quarter century of collisionless shock research. *Washington DC American Geophysical Union Geophysical Monograph Series*, 34:1–36, 1985.
- [26] M.G. Kivelson and C.T. Russell. *Introduction to space physics*. Cambridge atmospheric and space science series. Cambridge University Press, 1995.
- [27] A. Klassen, R. Gómez-Herrero, R. Müller-Mellin, S. Böttcher, B. Heber, R. Wimmer-Schweingruber, and G. M. Mason. STEREO/SEPT observations of upstream particle events: almost monoenergetic ion beams. *Annales Geophysicae*, 27:2077–2085, May 2009.
- [28] B. Klecker, H. Kunow, H. V. Cane, S. Dalla, B. Heber, K. Kecskemety, K.-L. Klein, J. Kota, H. Kucharek, D. Lario, M. A. Lee, M. A. Popecki, A. Posner, J. Rodriguez-Pacheco, T. Sanderson, G. M. Simnett, and E. C. Roelof. Energetic Particle Observations. *Space Science Reviews*, 123:217–250, March 2006.
- [29] S. M. Krimigis, C. O. Bostrom, T. P. Armstrong, W. I. Axford, C. Y. Fan, G. Gloeckler, and L. J. Lanzerotti. The Low Energy Charged Particle /LECP/ experiment on the Voyager spacecraft. *Space Science Reviews*, 21:329–354, December 1977.
- [30] H. Kucharek and E. Möbius. Ion Dynamics at Shocks: Ion Reflection and Beam Formation at Quasi-perpendicular Shocks. In G. Li, G. P. Zank, & C. T. Russell, editor, *The Physics of Collisionless Shocks: 4th Annual IGPP International Astrophysics Conference*, volume 781 of *American Institute of Physics Conference Series*, pages 32–36, August 2005.
- [31] M. A. Lee and L. A. Fisk. Shock acceleration of energetic particles in the heliosphere. *Space Science Reviews*, 32:205–228, March 1982.

- [32] M. A. Lee, V. D. Shapiro, and R. Z. Sagdeev. Pickup ion energization by shock surfing. *Journal of Geophysics Research*, 101:4777–4790, March 1996.
- [33] H. Li, C. Wang, and J. D. Richardson. Properties of the termination shock observed by Voyager 2. *Geophysics Research Letters*, 35:19107, October 2008.
- [34] P. C. Liewer, V. K. Decyk, J. M. Dawson, and B. Lembege. Numerical studies of electron dynamics in oblique quasi-perpendicular collisionless shock waves. *Journal of Geophysics Research*, 96:9455–9465, June 1991.
- [35] A. S. Lipatov, G. P. Zank, and H. L. Pauls. The acceleration of pickup ions at shock waves: Test particle-mesh simulations. *Journal of Geophysics Research*, 103:29679–29696, December 1998.
- [36] W. A. Livesey, C. T. Russell, and C. F. Kennel. A comparison of specularly reflected gyrating ion orbits with observed shock foot thicknesses. *Journal of Geophysics Research*, 89:6824–6828, August 1984.
- [37] E. Moebius. Pick-up of interstellar neutrals by the solar wind. *Advances in Space Research*, 6:199–208, 1986.
- [38] M. Neugebauer and J. Giacalone. Multispacecraft observations of interplanetary shocks: Nonplanarity and energetic particles. *Journal of Geophysical Research (Space Physics)*, 110:12106, December 2005.
- [39] G.K. Parks. *Physics Of Space Plasmas: An Introduction*. Westview Press, 2003.
- [40] A. Posner, N. A. Schwadron, D. J. McComas, E. C. Roelof, and A. B. Galvin. Suprathermal ions ahead of interplanetary shocks: New observations and critical instrumentation required for future space weather monitoring. *Space Weather*, 2:4, October 2004.

- [41] J. D. Richardson. Plasma temperature distributions in the heliosheath. *Geophysics Research Letters*, 35:23104, December 2008.
- [42] J. D. Richardson, J. C. Kasper, C. Wang, J. W. Belcher, and A. J. Lazarus. Cool heliosheath plasma and deceleration of the upstream solar wind at the termination shock. *Nature*, 454:63–66, July 2008.
- [43] C. T. Russell, L. K. Jian, X. Blanco-Cano, and J. G. Luhmann. STEREO observations of upstream and downstream waves at low Mach number shocks. *Geophysics Research Letters*, 36:3106, February 2009.
- [44] C. T. Russell, L. K. Jian, X. Blanco Cano, J. G. Luhmann, and T. L. Zhang. STEREO observations of shock formation in the solar wind. *Geophysics Research Letters*, 36:2103, January 2009.
- [45] T. R. Sanderson. ISEE-3 observations of energetic protons associated with interplanetary shocks. *Advances in Space Research*, 4:305–313, 1984.
- [46] C.J. Schrijver and G.L. Siscoe. *Heliophysics: space storms and radiation : causes and effects*. Heliophysics 3 Volume Set. Cambridge University Press, 2010.
- [47] N. Sckopke, G. Paschmann, S. J. Bame, J. T. Gosling, and C. T. Russell. Evolution of ion distributions across the nearly perpendicular bow shock - Specularly and non-specularly reflected-gyrating ions. *Journal of Geophysics Research*, 88:6121–6136, August 1983.
- [48] J. D. Scudder, T. L. Aggson, A. Mangeney, C. Lacombe, and C. C. Harvey. The resolved layer of a collisionless, high beta, supercritical, quasi-perpendicular shock wave. I - Rankine-Hugoniot geometry, currents, and stationarity. *Journal of Geophysics Research*, 91:11019–11052, October 1986.
- [49] V. M. Vasyliunas and G. L. Siscoe. On the flux and the energy spectrum of interstellar ions in the solar system. *Journal of Geophysics Research*, 81:1247–1252, March 1976.

- [50] F. Vesely. *Computational Physics: An Introduction*. Kluwer Academic/Plenum Publishers, 2001.
- [51] L. Wang, R. P. Lin, D. E. Larson, and J. G. Luhmann. Domination of heliosheath pressure by shock-accelerated pickup ions from observations of neutral atoms. *Nature*, 454:81–83, July 2008.
- [52] G. M. Webb, W. I. Axford, and T. Terasawa. On the drift mechanism for energetic charged particles at shocks. *Astrophysical Journal*, 270:537–553, July 1983.
- [53] K.-P. Wenzel. Charged particle acceleration processes in the interplanetary medium. *Advances in Space Research*, 9:179–190, 1989.
- [54] J. R. Wygant, M. Bensadoun, and F. S. Mozer. Electric field measurements at sub-critical, oblique bow shock crossings. *Journal of Geophysics Research*, 92:11109–11121, October 1987.
- [55] G. P. Zank, H. L. Pauls, I. H. Cairns, and G. M. Webb. Interstellar pickup ions and quasi-perpendicular shocks: Implications for the termination shock and interplanetary shocks. *Journal of Geophysics Research*, 101:457–478, January 1996.
- [56] G.P. Zank. Interaction of the solar wind with the local interstellar medium: a theoretical perspective. *Space Science Reviews*, 89:413–688, 1999. 10.1023/A:1005155601277.
- [57] D. Zilbersher and M. Gedalin. Pickup ion dynamics at the structured quasi-perpendicular shock. *Planetary Space Science*, 45:693–703, June 1997.